


8-2016

Mathematical hybrid models for image segmentation.

Carlos M. Paniagua Mejia

Follow this and additional works at: <https://ir.library.louisville.edu/etd>

 Part of the [Other Applied Mathematics Commons](#), and the [Partial Differential Equations Commons](#)

Recommended Citation

Paniagua Mejia, Carlos M., "Mathematical hybrid models for image segmentation." (2016). *Electronic Theses and Dissertations*. Paper 2534.

<https://doi.org/10.18297/etd/2534>

This Doctoral Dissertation is brought to you for free and open access by ThinkIR: The University of Louisville's Institutional Repository. It has been accepted for inclusion in Electronic Theses and Dissertations by an authorized administrator of ThinkIR: The University of Louisville's Institutional Repository. This title appears here courtesy of the author, who has retained all other copyrights. For more information, please contact thinkir@louisville.edu.

MATHEMATICAL HYBRID MODELS FOR IMAGE SEGMENTATION

By

Carlos M. Paniagua Mejía
BS, Instituto Tecnológico de Santo Domingo, 2004
MA, Instituto Tecnológico de Santo Domingo, 2008

A Dissertation
Submitted to the Faculty of the
College of Arts and Sciences of the University of Louisville
in Partial Fulfillment of the Requirements
for the Degree of

Doctor of Philosophy
in
Applied and Industrial Mathematics

Department of Mathematics
University of Louisville
Louisville, KY

August 2016

MATHEMATICAL HYBRID MODELS FOR IMAGE SEGMENTATION

Submitted by

Carlos M. Paniagua Mejía

A Dissertation Approved on

July 1, 2016

by the following Dissertation Committee:

Dr. Yongzhi Steve Xu, Dissertation
Director

Dr. Prasanna Sahoo

Dr. Changbing Hu

Dr. Douglas Lorenz

To Sarah

ACKNOWLEDGEMENTS

I am thankful to my advisor Dr. Yongzhi Steve Xu for his supervision of this thesis. He introduced me to applied problems of partial differential equations and the calculus of variations. His guidance, encouragement, and patience have been instrumental to the completion of this work.

I am also thankful to my advising committee: Dr. Prasanna Sahoo, Dr. Changbing Hu, and Dr. Douglas Lorenz. Special thanks to Dr. Thomas Riedel and Dr. Ryan Gill for their service to graduate students and their spirit to help in everything they could.

Finally, I am deeply grateful to my family, particularly to my mother Angélica and my wife Sarah, for their support and encouragement throughout all these years.

ABSTRACT

MATHEMATICAL HYBRID MODELS FOR IMAGE SEGMENTATION

Carlos M. Paniagua Mejía

May 24, 2016

Two hybrid image segmentation models that are able to process a wide variety of images are proposed. The models take advantage of global (region) and local (edge) data of the image to be segmented. The first one is a region-based PDE model that incorporates a combination of global and local statistics. The influence of each statistic is controlled using weights obtained via an asymptotically stable exponential function. Through incorporation of edge information, the second model extends the capabilities of a strictly region-based variational formulation, making it able to process more general images. Several examples are provided showing the improvements of the proposed models over recent methods along with an application to dermoscopy imaging. A number of avenues for future research are also discussed.

TABLE OF CONTENTS

1. INTRODUCTION	1
1.1 Parametric Models	2
1.1.1 Variational Analysis of the model	3
1.2 Geometric Models	6
1.2.1 Geometric heat flows	7
1.2.2 Weighting the arc length	8
1.2.3 Level set representation	11
1.3 Other models	14
1.4 Organization of this Thesis	16
2. A HYBRID PDE-BASED MODEL FOR BOUNDARY DETECTION . .	17
2.1 Prior works	17
2.2 Proposition of a new model	18
2.2.1 Goals and objectives	18
2.2.2 Model description and formulation	19
2.3 Discretization of the model	23
2.4 Experiments	25
2.5 Further Experiments	31
2.5.1 Performance on multimodal images	31
2.5.2 Images with Nonuniform Illumination	33
3. A HYBRID VARIATIONAL MODEL FOR BOUNDARY DETECTION .	35
3.1 Preliminaries	35
3.2 Model Formulation	37

3.3	Velocity Fields of Region Functionals	38
3.3.1	Converting Region Integrals to Boundary integrals	39
3.3.2	Computation of the Gateaux derivative	39
3.3.3	Construction of the velocity field for the solution of $\min E$	42
3.4	Numerical Implementation	43
3.5	Simulations	46
3.5.1	Application to Wider Class of Images	46
3.6	Further Experiments	47
3.6.1	Sensitivity to Initialization	48
3.6.2	Performance on multimodal images	49
3.6.3	Sensitivity to Noise	52
4.	LESION DETECTION IN DERMOSCOPY IMAGES	53
4.1	Segmentation of Dermoscopy Images	54
4.1.1	Proposed Methodology	55
4.1.2	Performance Metric	55
4.2	Simulations	56
5.	CONCLUSIONS AND FUTURE RESEARCH	60
	REFERENCES	63
	APPENDIX: MATLAB CODE	
A.	MATLAB CODE	69
A.1	PDE-based Model	69
A.2	Variational Model	74
B.	Frequently Used Symbols	80
	CURRICULUM VITAE	81

LIST OF TABLES

4.1	Segmentation error for images considered in Section 4.2.	59
-----	--	----

LIST OF FIGURES

1.1	An image I (on the left) and a blurred version $G_\sigma * I$, $\sigma = 1$. . .	11
2.1	Global image information vs. Local image information.	20
2.2	A “stretched” exponential $T(x) = 1 - e^{x/\nu}$ with $\nu = 43$	23
2.3	Pixel classification according to location within image.	25
2.4	An image that poses a relatively simple segmentation problem.	27
2.5	Robustness to initial condition.	28
2.6	Sensitivity to noise and <i>noisy</i> features	29
2.7	Proposed model applied to an MRI image.	30
2.8	Three special images.	31
2.9	Unsuccessful segmentation of multimodal image	32
2.10	Graylevel histograms for ‘coin’ and ‘four object’ images	32
2.11	Intensity mean inside front c_1 as function of number of iterations for ‘four-object’ image	33
2.12	Segmentation of ‘monkey’ image by PDE-base model	34
3.1	Composition of a bimodal image.	36
3.2	Incorrect segmentation using Separation of Means.	37
3.3	3×3 neighborhood of pixel (i, j)	45
3.4	Successful segmentation of ‘monkey’ image by our proposed model.	47
3.5	A successful segmentation of ‘galaxy’ image by our proposed model.	48
3.6	Segmentation results for ‘two cells’ image.	48
3.7	Sensitivity to initialization for the proposed variational model.	50

3.8	Segmentation of trimodal image with triple junction.	51
3.9	Selective segmentation in trimodal image with triple junction.	51
3.10	Segmentation of image with 4 regions	51
3.11	Effect of noise.	52
4.1	Some of the challenges of dermoscopy image segmentation. . .	54
4.2	Dermoscopy image with thick hair.	57
4.3	Dermoscopy image with thinner hair.	57
4.4	Dermoscopy image with sparse presence of hair and bubbles. .	58
4.5	Dermoscopy image with irregular skin around lesion.	58
4.6	Dermoscopy image of lesion with ambiguous boundary.	59
4.7	Image of lesion with significant color variation	59

CHAPTER 1

INTRODUCTION

Ever since the advent of computers an interest in equipping these devices with human-like capabilities has been a constant staple in the fields of Image Processing and Computer Vision. In particular, it is of interest to have a computer process an image in order to obtain a *meaningful* partition of its constituent objects. This is the basic problem in the subfield of Image Segmentation, and it has proven to be a challenging one due to the complexities present in images, and the imperfections introduced by the mechanisms through which images are obtained [17,62].

Over the past 25 years, beginning with the seminal works of Kass, et al. [27], and Mumford and Shah [41], an ever increasing number of Variational and partial differential equation (PDE) based methods (often termed *Deformable models* or *Active Contours*) for image segmentation have been proposed. The basic idea is to overlay a contour over the given image and evolve it so that it stops at the boundaries of relevant objects present in the image. This is typically accomplished by minimizing some kind of *energy* functional. Many other classical (non-PDE) approaches to the problem such as *thresholding* and *local filtering* (see e.g. [26]) have also been introduced. However, there is no unifying theory within the field, and as a result, most methods can only render satisfactory segmentation results for specific classes of images (see the discussion in [37, p. 367]). Our goal is to propose an overarching image segmentation scheme that is able to segment two very important classes of images: piecewise constant images, and inhomogeneous images which appear quite frequently in the medical sciences [17,23].

This chapter introduces the preliminary background necessary for the reader to completely comprehend and appreciate the results presented in this thesis. We start with a review of curve evolution, and present a thorough description of two relevant models (one Parametric and one Geometric) for object detection. Subsequently, we provide a brief overview of the level set method, and conclude with a discussion on PDE-based models.

In what follows, and throughout this dissertation we represent by Ω a bounded and open subset of the plane \mathbb{R}^2 . The grayscale image I to be segmented is realized as a bounded real valued function defined on Ω , $I : \Omega \rightarrow \mathbb{R}$. In image processing tasks such as image segmentation $\bar{\Omega}$ is typically a rectangle $[0, a] \times [0, b]$, and I is a discrete function taking values from 0 to 255. The number $I(\mathbf{x}) = I(x, y)$ is called the graylevel or intensity of I at the *pixel* $\mathbf{x} = (x, y) \in \Omega$. Let $C = C(q, t) : [0, 1] \times [0, \infty) \rightarrow \Omega$ be a smooth family of closed planar curves where q parameterizes the curve $C(\cdot, t)$ and t parameterizes the family.

1.1 Parametric Models

The first variational model for image segmentation was proposed by Kass, Witkin, and Terzopoulos in the late 1980's [27]. Their idea consisted on overlaying the image with a curve and allow the curve to deform until it conforms to the boundaries of relevant objects present in the image. *Forces* that propagate the curve are specified by the image itself in the form of a *potential*. Marr and Hildreth in their *Theory of Edge Detection* [38] argue that objects' contours occur at irregular parts of an image. In particular, one expects significant changes in image intensity across an ideal edge. To this end in [27] a very simple potential in terms of the gradient vector of I is proposed for edge detection:

$$P(\mathbf{x}) = -\|\nabla I(\mathbf{x})\|^2. \tag{1.1}$$

Using this potential, we can define the functional

$$E_{ext}(C) = \int_0^1 P(\mathbf{x})dq. \quad (1.2)$$

and seek curves C that make (1.2) as small as possible. However, minimizers of (1.2) are not guaranteed to be well-defined curves, so other terms ought to be added to (1.2) in order to control the regularity of the minimizer C . If we envision C as a thin membrane, we can exert control over its *rigidity* using the *internal* energy

$$E_{int}(C) = \frac{1}{2} \int_0^1 \left(\alpha \|C'(q)\|^2 + \beta \|C''(q)\|^2 \right) dq \quad (1.3)$$

where $\alpha, \beta > 0$ and the primes represent derivatives with respect to the parameter q ¹. The full energy is then

$$\begin{aligned} E(C) &= E_{int}(C) + E_{ext}(C) \\ &= \int_0^1 \left(\frac{\alpha}{2} \|C'(q)\|^2 + \frac{\beta}{2} \|C''(q)\|^2 + P(\mathbf{x}) \right) dq \end{aligned} \quad (1.4)$$

1.1.1 Variational Analysis of the model

The problem of minimizing (1.4) is stated in *weak* form. To obtain a minimizer, assuming one exists, we restate the problem in its *strong* form using the *Calculus of Variations*. This is, we take the *first variation*, Gateaux derivative, or functional derivative [4, 5, 53] of E with respect to t . Before this, we pause to obtain the time derivatives for each of the terms in the integrand of (1.4). In its most explicit form the curve C can be written as a vector in \mathbb{R}^2 as $C(q, t) = \langle x(q, t), y(q, t) \rangle$, where $x(q, t)$ and $y(q, t)$ are real valued functions of $q \in [0, 1]$ and $t \geq 0$. Then

$$\|C'(q)\|^2 = (x_q(q, t))^2 + (y_q(q, t))^2$$

¹We shall use the usual notation for partial derivatives: For the function $x(q, t)$, we represent by $x_q(q, t)$ and $x_t(q, t)$ its derivatives with respect to q and t , respectively.

and

$$\begin{aligned}\frac{d}{dt}\|C'(q)\|^2 &= 2(x_q x_{qt} + y_q y_{qt}) \\ &= 2C_q \cdot C_{qt}.\end{aligned}\tag{1.5}$$

Similarly,

$$\|C''(q)\|^2 = (x_{qq})^2 + (y_{qq})^2$$

and its derivative is

$$\begin{aligned}\frac{d}{dt}\|C''(q)\|^2 &= 2(x_{qq}x_{qqt} + y_{qq}y_{qqt}) \\ &= 2C_{qq} \cdot C_{qqt}.\end{aligned}\tag{1.6}$$

Finally, the derivative of the potential is

$$\frac{d}{dt}P(\mathbf{x}) = \nabla P \cdot C_t.\tag{1.7}$$

We are now ready to obtain the first variation of (1.4). Differentiating (1.4) we get

$$\begin{aligned}\frac{dE}{dt} &= \frac{d}{dt} \int_0^1 \left(\frac{\alpha}{2} \|C'(q)\|^2 + \frac{\beta}{2} \|C''(q)\|^2 + P(\mathbf{x}) \right) dq \\ &= \int_0^1 \frac{d}{dt} \left(\frac{\alpha}{2} \|C'(q)\|^2 + \frac{\beta}{2} \|C''(q)\|^2 + P(\mathbf{x}) \right) dq \\ &= \int_0^1 \left(\frac{\alpha}{2} \frac{d}{dt} \|C'(q)\|^2 + \frac{\beta}{2} \frac{d}{dt} \|C''(q)\|^2 + \frac{d}{dt} P(\mathbf{x}) \right) dq\end{aligned}\tag{1.8}$$

and using (1.5)–(1.7) in (1.8) after some simplification we arrive to

$$\frac{dE}{dt} = \int_0^1 (\alpha C_q \cdot C_{qt} + \beta C_{qq} \cdot C_{qqt} + \nabla P \cdot C_t) dq.\tag{1.9}$$

To get the strong form (Euler equation) we need to *raise* C_{qt} and C_{qqt} in the first two terms of (1.9) to C_t . We do this using integration by parts on the q variable.

To do this we recall that the curves $C(\cdot, t)$ are closed, so the following conditions

hold for C and its derivatives:

$$\begin{aligned}
C(0, t) &= C(1, t) \\
C_q(0, t) &= C_q(1, t) \\
C_{qq}(0, t) &= C_{qq}(1, t) \\
C_{qqq}(0, t) &= C_{qqq}(1, t)
\end{aligned} \tag{1.10}$$

After integrating by parts (1.9) once, we obtain

$$\begin{aligned}
\frac{dE}{dt} &= \alpha \left(C_q \cdot C_t \Big|_0^1 - \int_0^1 C_{qq} \cdot C_t dq \right) + \beta \left(C_{qq} \cdot C_{qt} \Big|_0^1 - \int_0^1 C_{qt} \cdot C_{qqq} dq \right) \\
&\quad + \int_0^1 \nabla P \cdot C_t dq
\end{aligned}$$

which simplifies to

$$\frac{dE}{dt} = \int_0^1 (-\alpha C_{qq} \cdot C_t - \beta C_{qqq} \cdot C_{qt} + \nabla P \cdot C_t) dq \tag{1.11}$$

after using conditions (1.10). Integrating by parts once more (on the middle term only) we have

$$\frac{dE}{dt} = \int_0^1 -\alpha C_{qq} \cdot C_t dq - \beta \left(C_{qqq} \cdot C_t \Big|_0^1 - \int_0^1 C_{qqqq} \cdot C_t dq \right) + \int_0^1 \nabla P \cdot C_t dq,$$

and by (1.10) for the third order derivative of C we arrive to

$$\begin{aligned}
\frac{dE}{dt} &= \int_0^1 (-\alpha C_{qq} \cdot C_t + \beta C_{(iv)} \cdot C_t + \nabla P \cdot C_t) dq \\
&= \int_0^1 (-\alpha C_{qq} + \beta C_{(iv)} + \nabla P) \cdot C_t dq,
\end{aligned} \tag{1.12}$$

where $C_{(iv)} = C_{qqqq}$. At a minimum (1.12) must be zero, and this is so if and only if the integrand (with C_t not identically zero) is zero. This observation yields the strong form of (1.4)

$$-\alpha C_{qq} + \beta C_{(iv)} + \nabla P = 0 \tag{1.13}$$

with boundary conditions (1.10). As the terms of energy (1.4) are quadratic, equation (1.13) is a linear partial differential equation. Its solution can be approximated

using Gradient (or Steepest) descent method. This is accomplished by converting and elliptical-type problem to a parabolic one. For problem (1.13) we can write

$$C_t = -\alpha C_{qq} + \beta C_{(iv)} + \nabla P \quad (1.14)$$

so that the steady state of (1.14), that is, when $C_t = 0$, renders the solution of (1.13).

At this point we make a few remarks about this model:

- a) Due to dependency of the chosen parametrization of the initial curve $C(q, t)|_{t=0}$ different solutions may be obtained under a parametrization $C(p, t)|_{t=0}$, even with $C(q, t)|_{t=0} = C(p, t)|_{t=0}$.
- b) Due to shape constraints (1.3) the curves $C(q, t), t > 0$ are to be very similar to $C(q, t)|_{t=0^-}$ in particular, changes in topology cannot be handled.

1.2 Geometric Models

Geometric models for image segmentation are based on techniques from the fields of differential geometry and geometric partial differential equations. Stemming from such formal branches of mathematics, geometric models for shape analysis enjoy theoretical robustness and some existence, uniqueness, and numeric results have being obtained [2]. Most geometric models, unlike the parametric model just presented, are not formulated via an energy minimization problem [3, 6, 36, 66]. These were proposed, preeminently, to overcome the weaknesses of the parametric model presented on the previous section [6, 7]. In order to illustrate the main ideas underpinning these models, in this section we present a fairly detailed description of one of the most important geometric models for image segmentation.

1.2.1 Geometric heat flows

For the planar curve $C(q, t)$, we denote by $\kappa = \kappa(x, y)$, $\vec{T} = \vec{T}(x, y)$, and $\vec{N} = \vec{N}(x, y)$, respectively, the curvature, the unit tangent vector, and *principal* inward unit normal vector at the point (x, y) . These parameters have explicit representation

$$\vec{T} = \frac{C_q}{\|C_q\|}, \quad \vec{N} = \frac{\vec{T}_q}{\|\vec{T}_q\|}, \quad \kappa = \frac{\|\vec{T}_q\|}{\|C_q\|}. \quad (1.15)$$

With this notation, we introduce the *geometric heat equation*

$$C_t = \kappa \vec{N}. \quad (1.16)$$

This equation prescribes the motion of the points of C along the normal direction with velocity the curvature κ . We are going to show that this flow reduces the arc length of C as quickly as possible. Let us denote by $L(t)$ the arc length of C at time t . Then, by definition of arc length

$$L(t) = \oint_C ds = \int_0^1 \|C_q\| dq.$$

As stated before, C (and its first order partial derivatives with respect to q and t) being a closed curve satisfies the boundary conditions

$$\begin{aligned} C(0, t) &= C(1, t) \\ C_q(0, t) &= C_q(1, t) \\ C_t(0, t) &= C_t(1, t) \end{aligned} \quad (1.17)$$

Computing the Gateaux derivative (or *first variation*) of the arc length functional we get

$$\frac{d}{dt}L(t) = L'(t) = \int_0^1 \frac{d}{dt} \|C_q\| dq = \int_0^1 \frac{C_q \cdot C_{qt}}{\|C_q\|} dq = \int_0^1 \frac{C_q}{\|C_q\|} \cdot C_{qt} dq. \quad (1.18)$$

In view of (1.16), we want to obtain an equivalent formulation of (1.18) with its integrand a product involving C_t . In this way, by the theory of the calculus of

variations and steepest descent, we can define a flow of C , that is C_t , with its right hand side the other factor involved in the integrand. To this end we integrate (1.18) by parts with respect to q so that

$$\begin{aligned}
L'(t) &= \int_0^1 \frac{C_q}{\|C_q\|} \cdot C_{qt} dq \\
&= \int_0^1 \vec{T} \cdot C_{qt} dq = \left. \frac{C_q}{\|C_q\|} \cdot C_t \right|_0^1 - \int_0^1 C_t \cdot \vec{T}_q dq \\
&= - \int_0^1 C_t \cdot \vec{T}_q dq \\
&= - \int_0^1 (C_t \cdot \frac{\vec{T}_q}{\|C_q\|}) \|C_q\| dq.
\end{aligned}$$

where we have used the boundary conditions (1.17) and multiplied and divided by the scalar $\|C_q\|$. By formulas (1.15) and parameterizing with respect to arc length we arrive to

$$L'(t) = - \int_0^{L(t)} C_t \cdot \kappa \vec{N} ds, \quad (1.19)$$

where $ds := \|C_q\|dq$. It is now evident that $L(t)$ decreases most rapidly when $C_t = \kappa \vec{N}$, as claimed.

The flow (1.16) is called (for good reason) the *shortening flow*. These types of flows are the most important for image segmentation as we would like the object delimiting contours to have minimal length.

1.2.2 Weighting the arc length

In [28] Kichenassamy et al., proposed to redefine the arc length of C by *weighting* the infinitesimal element of length ds with a positive differentiable function $g(x, y)$. For the purposes of shape detection this function ought to be chosen according to the properties of the image to be segmented. For now it is only assumed that g is smooth so that a steepest descent flow for the weighted arc length can be obtained in a similar way as in the previous section. The new flow is obtained as follows: the

weighed arc length is defined as

$$ds_g = g ds = g(x, y) \|C_q\| dq, \quad (1.20)$$

so that the total weighted arc length of C is

$$L_g(t) = \int_0^1 \|C_q\| g dq. \quad (1.21)$$

We now compute the first variation of (1.21) to get

$$\frac{d}{dt} L_g(t) = L'_g(t) = \int_0^1 \frac{d}{dt} [\|C_q\| g] dq. \quad (1.22)$$

Note that

$$\frac{d}{dt}(g(x, y)) = g_x x_t + g_y y_t = \nabla g \cdot C_t \quad (1.23)$$

Then (1.22) becomes

$$\begin{aligned} L'_g(t) &= \int_0^1 \frac{d}{dt} [\|C_q\| g] dq = \int_0^1 \left[g \vec{T} \cdot C_{qt} + \|C_q\| (\nabla g \cdot C_t) \right] dq \\ &= \int_0^1 \underline{g \vec{T} \cdot C_{qt}} dq + \int_0^1 (\nabla g \cdot C_t) \|C_q\| dq. \end{aligned} \quad (1.24)$$

Integrating the underlined term in the right hand side of (1.24) by parts we get

$$L'_g(t) = \underline{g \vec{T} \cdot C_t} \Big|_0^1 - \int_0^1 C_t \cdot \frac{\partial}{\partial q} (g \vec{T}) dq + \int_0^1 (\nabla g \cdot C_t) \|C_q\| dq. \quad (1.25)$$

We assume that the conditions (1.17) remain valid, so the underlined term in (1.25)

vanishes. For the derivative in the middle term we note that $\vec{T}_q = \|C_q\| \kappa \vec{N}$. Thus,

$$\begin{aligned} L'_g(t) &= - \int_0^1 C_t \cdot \left[(\nabla g \cdot C_q) \vec{T} + g \|C_q\| \kappa \vec{N} \right] dq + \int_0^1 (\nabla g \cdot C_t) \|C_q\| dq \\ &= - \int_0^1 C_t \cdot \left[(\nabla g \cdot \vec{T}) \vec{T} + g \kappa \vec{N} - \nabla g \right] \|C_q\| dq \end{aligned} \quad (1.26)$$

where we have used the fact that $(\nabla g \cdot C_q) \vec{T} = (\nabla g \cdot \vec{T}) \vec{T} \|C_q\|$. Therefore, the weighted arc length $L_g(t)$ decreases most rapidly when

$$C_t = g \kappa \vec{N} + (\nabla g \cdot \vec{T}) \vec{T} - \nabla g. \quad (1.27)$$

The middle term in the right hand side of (1.27) can be removed as tangential components of velocities do not affect the deformation of planar curves. This result is referred to as the Epstein-Gage lemma. We state this lemma whose proof can be found in [19].

Lemma 1.1. *Let $C(\tilde{q}, t) : S \times [0, T] \rightarrow \mathbb{R}^2$ be a family of closed embedded curves that obeys the pde:*

$$\begin{aligned} C_t(\tilde{p}, t) &= \alpha(\tilde{p}, t)\vec{T}(\tilde{p}, t) + \beta(\tilde{p}, t)\vec{N}(\tilde{p}, t), \\ C(\tilde{p}, 0) &= C_0(\tilde{p}), \end{aligned} \tag{1.28}$$

for some initial curve $C(\tilde{p}, 0)$. If the normal component of speed β does not depend on the parameterization, then the curve $C(\tilde{p}, t)$ that satisfies (1.28) is identical to the family of curves $C(p, t)$ that satisfies

$$C_t(p, t) = \beta(p, t)\vec{N}(p, t). \tag{1.29}$$

In view of Lemma 1.1, the model in (1.27) reduces to

$$C_t = g\kappa\vec{N} - \nabla g. \tag{1.30}$$

One hopes that the steady state of (1.30) will render a meaningful segmentation of the given image. The *edge-stopping function* g acts on the image I , so that its value becomes small at discontinuities of I . For example, in [28] (and other works cited therein), the authors use

$$g = \frac{1}{1 + \|\nabla G_\sigma * I\|^n} \tag{1.31}$$

where $n = 1, 2$. $G_\sigma * I$ is the convolution of the image I with a Gaussian kernel $G_\sigma = \sigma^{-1/2}e^{-|\mathbf{x}|^2/4\sigma}$ with standard deviation σ (see Fig. 1.1).

A few remarks are in order. The model represented by (1.30) is nonlinear. As a result trying to prove existence and uniqueness of solutions for this type of equation in the classical sense is typically very hard or altogether avoided. Moreover, weak



Figure 1.1: An image I (on the left) and a blurred version $G_\sigma * I$, $\sigma = 1$. Some sharpness is removed from the original as a result of the operation.

(in the now *classical* sense) solutions are not possible either since (1.30) does not belong to the class of problems that can be written in divergence form (see [21], for example). Due to the great variety of objects and anomalies that may be present in an image, evolving contours are to develop singularities (contours may split to conform to edges, angles etc.) A different paradigm is thus needed as the solutions of PDEs such as (1.30) may not be everywhere differentiable. To this end, a new notion of weak solution was introduced by Evans in [20], and later expanded by Crandall and Lions in [15] in the early 1980's, that seems to be suitable to describe solutions of front propagation (a variant being addressed here) and optimal control problems. This new paradigm is the so-called sense of *viscosity solutions* (see for example [13–15]). We are going to be more concerned with numerical solutions of our models for which we employ the *level set method* first introduced by Sethian in [49], and further developed by Sethian and Osher in [44]. Benefits of this representation include automatic handling of changes in topology and self-intersections of the evolving contours (shocks). We do so for model (1.30) next.

1.2.3 Level set representation

If we embed the family of curves in the plane $C(x(q,t), y(q,t)) = C(x, y, t)$ (again, q parameterizes the curve for a given $t \geq 0$) as the zero (chosen for simplicity–

any level line c is adequate) level set of a Lipschitz continuous function u , we can describe C in terms of u as

$$C(x, y, t) = \mathfrak{L}_0 \equiv \{(x, y, t) : u(x, y, t) = 0\}. \quad (1.32)$$

For a fixed t , it is easy to see that $\|\nabla u\|$ is perpendicular to the tangent vector of C . This implies that the vectors $\vec{\mathcal{N}}$ and ∇u are orthogonal. This allows to define the inward unit normal vector $\vec{\mathcal{N}}$ to \mathfrak{L}_0 as

$$\vec{\mathcal{N}} = -\frac{\nabla u}{\|\nabla u\|}, \quad (1.33)$$

which leads to an equation for the curvature κ in terms of the level set curve u :

$$\kappa = \operatorname{div} \left(\frac{\nabla u}{\|\nabla u\|} \right) = \nabla \cdot \left(\frac{\nabla u}{\|\nabla u\|} \right). \quad (1.34)$$

In the classical level set method [49, 50] the typical choice for the embedding function u is the *signed distance function* to the curve C . For C a smooth, closed, planar curve, we denote its interior by $\operatorname{int}(C)$ and by $\partial\operatorname{int}(C)$ its boundary. We can define the signed distance function to the curve C as follows

$$u = u(\mathbf{x}) = \begin{cases} d(\mathbf{x}), & \mathbf{x} \in \operatorname{int}(C) \\ 0, & \mathbf{x} \in \partial\operatorname{int}(C) \\ -d(\mathbf{x}), & \mathbf{x} \notin \operatorname{int}(C) \end{cases}$$

where

$$d(\mathbf{x}) = \inf \|\mathbf{x} - \mathbf{y}\|, \text{ for all } \mathbf{y} \in \partial\operatorname{int}(C).$$

The choice of having positive distances on $\operatorname{int}(C)$ is arbitrary. However, for computational purposes that do not require the key property of signed distance functions, namely $\|\nabla u\| = 1$ [43] (see also [44, 49] for explanations as to why this property is desirable for certain applications), any function that is positive on $\operatorname{int}(C)$ and

negative on the outside of C are equally adequate and much simpler to compute [66]. For example, if one is only interested in tracking the zero level set we can define

$$u = \tilde{u}(\mathbf{x}) = \begin{cases} 1, & \mathbf{x} \in \text{int}(C) \\ 0, & \mathbf{x} \in \partial\text{int}(C) \\ -1, & \mathbf{x} \notin \text{int}(C) \end{cases} \quad (1.35)$$

Let us now present the evolution of the level sets of u as prescribed by (1.30) (shown below for convenience):

$$C_t = g\kappa\vec{\mathcal{N}} - \nabla g. \quad (1.36)$$

We differentiate u with respect to t . Thus, by the chain rule we have

$$\frac{d}{dt}(u(x, y, t)) = \nabla u \cdot C_t + u_t.$$

In view of (1.36), we get

$$\begin{aligned} g\kappa\vec{\mathcal{N}} \cdot \nabla u - \nabla g \cdot \nabla u + u_t &= 0 \\ \Rightarrow u_t &= -g\kappa\vec{\mathcal{N}} \cdot \nabla u + \nabla g \cdot \nabla u \end{aligned} \quad (1.37)$$

and using (1.33) and (1.34) in (1.37) we arrive, after a straightforward simplification, to

$$u_t = g \operatorname{div} \left(\frac{\nabla u}{\|\nabla u\|} \right) \|\nabla u\| + \nabla g \cdot \nabla u. \quad (1.38)$$

We now describe the contributions of each term of (1.38). The first term in the right hand side is the shortening term; it propagates (shrinks) u in the normal direction according to the velocity g . On the other hand, the term $\nabla g \cdot \nabla u$ stops the shrinking at objects' boundaries. Indeed, if the zero level set of u is near and inside an object with relative homogeneous gray level intensity, ∇u will point toward the exterior of the object where the change in gray level is the greatest.

From a practical standpoint model (1.36) (and (1.38) in the level set framework) has a number of weaknesses:

- a) This flow decreases arc length of $C(q, t)$ (or u). Therefore, the initial contour must surround the target objects of the image. However, some control can be exerted on this behavior. The contour can be made to expand (like a balloon [6]) by introducing a constant parameter c as follows:

$$u_t = g \left[\operatorname{div} \left(\frac{\nabla u}{\|\nabla u\|} \right) + c \right] \|\nabla u\| + \nabla g \cdot \nabla u. \quad (1.39)$$

In this way the arc length can be made to increase (according to the sign of c), so that the initial curve could be placed within the boundaries of the target objects.

- b) Since the model relies on an edge detector g to stop the propagation of the curves, boundaries in images consisting of weak edges may not be properly segmented. Typical examples are x-ray images, MRIs, military applications (radar) images.
- c) Presence of spurious objects, or *noise*, in images may hamper the effectiveness of the model, making preprocessing tasks such as *denoising* a necessity before conducting the segmentation task.

1.3 Other models

In this concluding section we briefly show yet another way in which shape reconstruction models can be formulated from a level set based formulation. We refer the reader to [6] for another classical example of these type of models. As before, we denote by u the level set function representation of a planar curve C as in (1.32). The basic idea here is to define appropriate speed functions F , depending on the given image I and initial curve $u(\mathbf{x}, t)|_{t=0}$, such that the equation

$$u_t + F \|\nabla u\| = 0 \quad (1.40)$$

attains steady state at the boundary of objects in images. In [36], for example, the proposed speed function is $F = F_A + F_I$ with

$$F_I = -\frac{F_A}{M_1 - M_2} (\|\nabla G_\sigma * I\| - M_2) \quad (1.41)$$

where F_A is a positive number, and M_1 and M_2 are, respectively, the maximum and minimum values of the image gradient $\|\nabla G_\sigma * I\|$, $0 \leq M_2 < M_1 < \infty$ (see page 10). Now

$$\begin{aligned} M_2 &\leq \|\nabla G_\sigma * I\| \leq M_1 \\ 0 &\leq \|\nabla G_\sigma * I\| - M_2 \leq M_1 - M_2 \\ 0 &\leq \frac{\|\nabla G_\sigma * I\| - M_2}{M_1 - M_2} \leq 1 \\ 0 &\leq \frac{F_A}{M_1 - M_2} (\|\nabla G_\sigma * I\| - M_2) \leq F_A \\ -F_A &\leq -\frac{F_A}{M_1 - M_2} (\|\nabla G_\sigma * I\| - M_2) \leq 0. \end{aligned}$$

This shows that the values of F_I are in the interval $[-F_A, 0]$ and those of F defined above in equation (1.41) are in the unit interval $[0, 1]$. These observations suggest that the evolution of u in equation (1.40) will stop at nearby object boundaries of the image I .

Speeds that depend on geometric properties of the evolving curve u can also be incorporated into model (1.40). In this way some control can be exerted over u to keep its evolution regular, in much the same way E_{int} regularizes the minimizer of the parametric model (1.4). Let this speed be denoted by F_G . Then F in (1.40) can be decomposed as

$$F = F_A + F_G + F_I. \quad (1.42)$$

For example, F_G can be defined as a function of mean curvature of u [22]. Although nice properties of the flow by mean curvature are inserted, steady state of the zero level set of (1.40) with F as in (1.42) cannot be attained at the boundary of objects

for additive image based forces F_I . A way to achieve this is by incorporating a factor, call it k_I depending on the image I , so that F becomes small at object's boundaries. This technique was described in subsection 1.2.2 when edge stopping functions were introduced. In this spirit, we make the image information be carried by the edge stopping factor k_I and make $F_I = 0$ in (1.42). The corresponding model is

$$u_t + k_I (F_A + F_G) \|\nabla u\| = 0, \quad (1.43)$$

with, for example, $k_I = g$ of equation (1.31).

1.4 Organization of this Thesis

The contributions of this thesis are twofold.

1. In Chapter 2 we present a PDE-based model for shape detection by directly specifying the differential equation. This model cannot be obtained from a variational formulation, and takes advantage of both local and global region statistics, whose contributions are balanced by edge information from the image.
2. Chapter 3 contains a variational formulation of a second model for image segmentation. The proposed model also incorporates edge information from image (in a different way the model in Chapter 2 does) and extends the capabilities of a pure region based model to process a large class of images.
3. In Chapter 4 we apply the proposed models to medical imaging. Particularly, the models are used to detect skin lesions in dermoscopy imagery.
4. Chapter 5 wraps up the dissertation and some avenues for future research are explored.

In the Appendix we include the code used for the implementation of both models.

CHAPTER 2

A HYBRID PDE-BASED MODEL FOR BOUNDARY DETECTION

2.1 Prior works

The fields Mathematical imaging, image processing, computer vision etc., deal with extracting information from images and giving their contents sensible interpretations. Typical operations include (see [37] for an exhaustive list) at *the low level*: noise removal, blurring and deblurring; at the *mid level*: edge detection, segmentation, and object tracking; and the *high level*: analysis and interpretation of a scene. We are concerned with the task of segmentation which at its core involves performing certain operations on a image to obtain a sort of map delineating the regions (or objects) present within this image. Once an image has been segmented, the resulting individual regions can be described, represented, analyzed, or classified, and the applications are too many to list here [23, 37, 40, 47].

Many techniques have been proposed to solve this problem over the past four decades and yet the segmentation problem remains unsolved. In the 1970's research mainly focused on methods such as *thresholding*, *region growing*, and *split and merge* algorithms, the majority of which were proposed by computer scientists and investigators from related fields [26, 38]. Later in the mid to late 1980's the first PDE-based methods entered the literature incorporating edge information from image in the form of gradients (chapter 1). These methods are often referred to as *edge-based methods*. Research continued on this front and in the late 1990's investigators

started to consider *region-based* information from images to make segmentation results more robust to noisy features and location of initial contours. Out of these are worth mentioning the works proposed by Chan and Vese [9], Yezzi et al. [65] and Li et al. [32–34]. Subsequently, *hybrid* approaches, incorporating both edge and region data, were introduced showing promising results. These include variational formulations (see for example [30, 63]) and more general (non-variational) PDE-based models [10, 11, 57, 66].

In this chapter, we present our first PDE-based model for image segmentation. We start by stating our goals with the proposition of the new model. We then proceed with its formulation and implementation, and conclude with some experiments to identify its strengths and limitations.

2.2 Proposition of a new model

2.2.1 Goals and objectives

Our goal is to obtain a more versatile model for image segmentation. From a practical standpoint, we seek to obtain meaningful segmentations not only for images with relatively well defined boundaries with piecewise smooth regions, but also for inhomogeneous images with varying regions in gray level and or whose objects are defined by somewhat weak edges. Further, we would like our model to be free of the weaknesses models (1.4) and (1.38) exhibit, namely, that it be more flexible in terms of the location of initial contours so that this could be located anywhere in the image domain, and that it be able to handle changes in topology of the evolution curve.

As we mentioned, the models described in the previous chapter belong to a class referred to as *Edge-based methods*. Region-based models, on the other hand, do not depend on edge information. Instead, they exploit statistical information carried by

the image. For example, given a subset (or region) \mathcal{U} of the image domain Ω , we can employ statistics such as the mean intensity of I within \mathcal{U}

$$\mu_{\mathcal{U}} = \frac{1}{|\mathcal{U}|} \int_{\mathcal{U}} I(\mathbf{x}) d\mathbf{x}, \quad (2.1)$$

where $|\mathcal{U}| = \int_{\mathcal{U}} d\mathbf{x}$ (the measure of \mathcal{U}), or the variance within \mathcal{U}

$$\sigma_{\mathcal{U}}^2 = \frac{1}{|\mathcal{U}|} \int_{\mathcal{U}} (\mu_{\mathcal{U}} - I(\mathbf{x}))^2 d\mathbf{x}. \quad (2.2)$$

We seek to incorporate both of these types of image data (edge information and global statistics) to obtain a *hybrid model*

$$u_t + F \|\nabla u\| = 0 \quad (2.3)$$

where $u = u(\mathbf{x}, t)$ represents the level sets of a family of curves $C(\mathbf{x}, t)$ (as in section 1.2.3) and the velocity field F is to incorporate both types of image information.

2.2.2 Model description and formulation

We draw inspiration from models proposed in [3, 6, 10, 36, 57, 66]. To specify our hybrid velocity, we are going to rely on three key assumptions:

ASSUMPTION 2.1. *The image gradient ∇I has relative large magnitude in a small neighborhood of a pixel \mathbf{x} at the boundary of an object.*

ASSUMPTION 2.2. *The image I to be segmented consists components of relatively piecewise constant gray level intensities.*

ASSUMPTION 2.3. *Mean values of I inside and outside an object of interest differ significantly in a neighborhood of a boundary pixel \mathbf{x} , even if the regions within I are not piecewise constant.*

The first assumption is typical of edge-based models. Assumption 2.2 is reasonable since one expects objects in (at least a wide class of) images to have the same

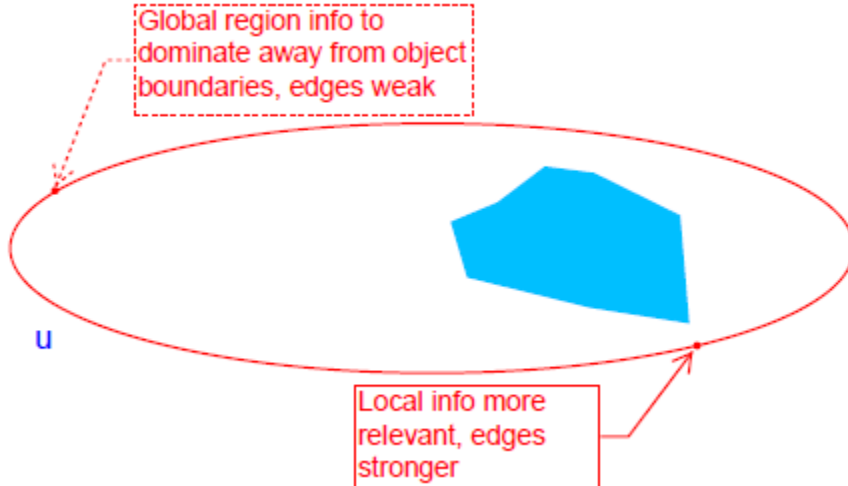


Figure 2.1: At a point \mathbf{x} on the evolution curve u the image gradient is expected to be smaller than at points \mathbf{y} that are close to objects of interest.

gray level within their boundaries, Fig. 2.1. And assumption 2.3 focuses the scope of assumption 2.2 to a neighborhood scale and should allow us to employ local statistics. We now proceed to define the velocity field F . The idea is to partition F into a weighted sum of two functionals

$$F = w_1 F_G + w_2 F_L$$

where F_G and F_L carry, respectively, global and local region information, and the weights w_1, w_2 are to carry edge information.

Region information Let U represent the interior of the zero level set curve u . The two operators $F_G(\cdot, \cdot)$ and $F_L(\cdot, \cdot)$ are defined as functions of the evolving level set curve u and carry statistical information of the image I according to the location of u . Their explicit representations are chosen as

$$\begin{aligned} F_G(u, I) &= \frac{2I - c_1 - c_2}{\max |2I - c_1 - c_2|} \\ F_L(u, I) &= \frac{2I - d_1 - d_2}{\max |2I - d_1 - d_2|}. \end{aligned} \tag{2.4}$$

Note that their dependency on u is implicit as the parameters c_1, c_2, d_1 , and d_2 are all functions of u . These are obtained using the formulas

$$c_1 = \frac{\int_U I(\mathbf{x})H(u)d\mathbf{x}}{\int_U H(u)d\mathbf{x}}; \quad c_2 = \frac{\int_U I(\mathbf{x})(1 - H(u))d\mathbf{x}}{\int_U (1 - H(u))d\mathbf{x}}; \quad (2.5)$$

$$d_1 = \frac{\int_W I(\mathbf{y})H(u)d\mathbf{y}}{\int_W H(u)d\mathbf{y}}; \quad d_2 = \frac{\int_W I(\mathbf{y})(1 - H(u))d\mathbf{y}}{\int_W (1 - H(u))d\mathbf{y}}. \quad (2.6)$$

where H is the standard Heaviside function defined by

$$H(x) = \begin{cases} 1, & x \geq 0 \\ 0, & x \leq 0 \end{cases},$$

and $W = W_\rho(\mathbf{x}) := \{\mathbf{y} \in \Omega \mid \mathbf{y} \in \|\mathbf{x} - \mathbf{y}\| \leq \rho, \mathbf{x} \in \partial U\}$, the region of pixels \mathbf{y} within distance $\rho \in \mathbb{N}$ of the pixel \mathbf{x} along the boundary of the curve u . Variants of forces (2.4) are common choices and have appeared before [66, 67].

If u is a signed distance function, or has the form of \tilde{u} as in (1.35), the four parameters in (2.5) and (2.6) above are averages of the image values I —global in the case of c_1 inside u , and c_2 outside of u , and local, in a neighborhood W of size ρ inside the image domain Ω centered at \mathbf{x} . Thus, the operators F_G and F_L attain values in the interval $[-1, 1]$. F_G expands u toward object boundaries when it lays on the interior of potential objects, and shrinks u when outside. F_L acts in a similar fashion but locally according to the window size ρ . A smaller value of ρ will strengthen the ability of F_L to capture object boundaries as finer variations are expected to be detected when a smaller ρ is used. We use edge data to combine the effects of these forces.

Edge information Edge data is typically associated to prominent variations of the image gradient $\|\nabla I\|$, ideally, jump discontinuities across an edge line. Further, if the evolving contour is far from the boundary of an object it is easy to see that the local statistics will not provide any new information about the object boundaries that is not already contained in the global statistics, that is

$c_i \approx d_i$, $i = 1, 2$. In other words, the global information is dominant when the evolving contour is far from an edge where small values $\|\nabla I\|$ are expected. On the other hand, when the c_i and d_i differ significantly, say $|c_i - d_i| \geq \delta$, for some threshold value $\delta > 0$, the relevance of the local and the global statistics are exchanged when the evolving contour is close to objects' boundaries (with presumably higher values of $\|\nabla I\|$) making the information carried by local statistics more relevant. Based on this observation, we can seek for increasing (1-to-1) functions of the image gradient $\nabla I(\mathbf{x})$ that approach 1 asymptotically:

$$\mathcal{F} := \{T : [0, \infty) \rightarrow R \mid T \text{ increasing}, T(0) = 0, \lim_{x \rightarrow \infty} T(x) = 1\}. \quad (2.7)$$

Note that $T(x) \in [0, 1]$ for $T \in \mathcal{F}$, so transformations in the family \mathcal{F} make for suitable candidates to balance the effects of the region information operators (2.4). In light of the previous discussion, we choose the *weights* w_1 and w_2 to be functions of the image gradient $\|\nabla I\|$ at each point $\mathbf{x} \in \Omega$, and are defined as follows¹ (see Fig. 2.2):

$$\begin{aligned} w_1 &= w_1(I(\mathbf{x})) = e^{-\|\nabla I\|/\nu}, \quad \nu > 0 \\ w_2 &= 1 - w_1. \end{aligned} \quad (2.8)$$

The proposed hybrid model for image segmentation is thus

$$u_t = \alpha [w_1 F_G(u, I) + w_2 F_L(u, I)] \|\nabla u\|, \quad (2.9)$$

with initial condition (chosen arbitrarily), $u(0, x, y) = u_0(x, y)$, with Neumann boundary conditions, and α is a positive constant intended to control the overall speed of propagation of the level sets of u . The operators $F_G(\cdot, \cdot)$, $F_L(\cdot, \cdot)$ and the weights w_1, w_2 are as in equations (2.4) and (2.8), respectively.

Before proceeding to its implementation, we make some remarks about our PDE-based model. First, the proposed model is region based. Edge information

¹We have chosen the transformation to be exponential for its simplicity. Other members of the family \mathcal{F} can be employed.

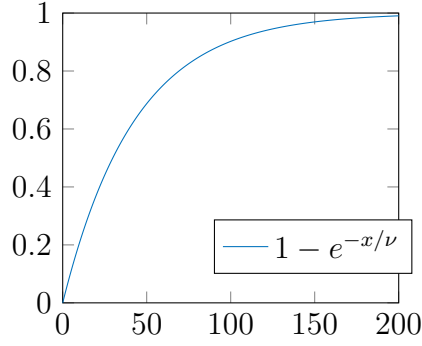


Figure 2.2: A “stretched” exponential $T(x) = 1 - e^{x/\nu}$ with $\nu = 43$.

is incorporated in the weights that control the interplay of local and global image statistics. Exploitation of both types of image data makes the model a hybrid model. And second, because our model does not include a curvature dependent term (see Section 1.2) which controls the arc length of the moving front, the model favors detection of finer regions as opposed to coarser ones. If larger scale segmentation is desired a curvature dependent term can be added to the right-hand side of (2.9).

2.3 Discretization of the model

The problem we need to solve, repeated below for convenience, is

$$\left\{ \begin{array}{l} u_t = \alpha [w_1 F_G(u, I) + w_2 F_L(u, I)] \|\nabla u\| \\ \frac{\partial u}{\partial \vec{n}} = 0 \text{ on } \partial\Omega \quad (\text{Neumann boundary condition}) \\ u(\mathbf{x}, 0) = u_0(\mathbf{x}) \quad (\text{initial condition}) \end{array} \right. \quad (2.10)$$

where $\Omega \subset R^2$ is the image domain, α a positive real number, \vec{n} the outer unit normal to $\partial\Omega$, the boundary of Ω . The operators $F_G(\cdot, \cdot)$, $F_L(\cdot, \cdot)$ and the weights w_1, w_2 are defined in equations (2.4) and (2.8), respectively.

To solve problem (2.10) we resort to a numerical solution. The underlying nature of the problem suggests implementation of a finite difference scheme. The image domain Ω is discretized into $N \times N$ points along both the x and y directions

each separated by increments of size h , so that

$$x_i = ih, \quad y_j = jh, \quad \text{for } i, j = 1, 2, \dots, N, \quad \text{and} \quad Nh = 1. \quad (2.11)$$

For the time direction we choose steps of size Δt so we define

$$t_n = n\Delta t, \quad \text{for } n = 0, 1, \dots \quad (2.12)$$

In this way the unknown function $u(\mathbf{x}, t)$ is approximated by

$$u_{ij}^n = u(x_i, y_j, t_n) \quad (2.13)$$

at each pixel $(ih, jh) = (i, j)$ for each time $n\Delta t$. The time derivative is estimated using first-order accurate forward differences

$$u_t = \frac{u_{ij}^{n+1} - u_{ij}^n}{\Delta t} \quad (2.14)$$

and the spatial derivatives are estimated using second-order accurate centered differences

$$\|\nabla u\|^2 = (u_x^2 + u_y^2)|_{ij}^n = \left(\frac{u_{i+1,j}^n - u_{i-1,j}^n}{2h} \right)^2 + \left(\frac{u_{i,j+1}^n - u_{i,j-1}^n}{2h} \right)^2 \quad (2.15)$$

for interior points $i, j = 2, 3, \dots, N - 1$. At boundary points $i, j = 1, N$ we employ forward/backward differences as necessary (Fig. 2.3). For example, at the left and top edges we use forward differences in the x and y directions, respectively. For pixels at the right and bottom boundaries we employ backward differences. This leads immediately to the following boundary conditions:

$$\begin{aligned} u_{2j}^n &= u_{1j}^n && \text{(top boundary)} \\ u_{N,j}^n &= u_{N-1,j}^n && \text{(bottom boundary)} \\ u_{i2}^n &= u_{i1}^n && \text{(left boundary)} \\ u_{i,N}^n &= u_{i,N-1}^n && \text{(right boundary)} \end{aligned} \quad (2.16)$$

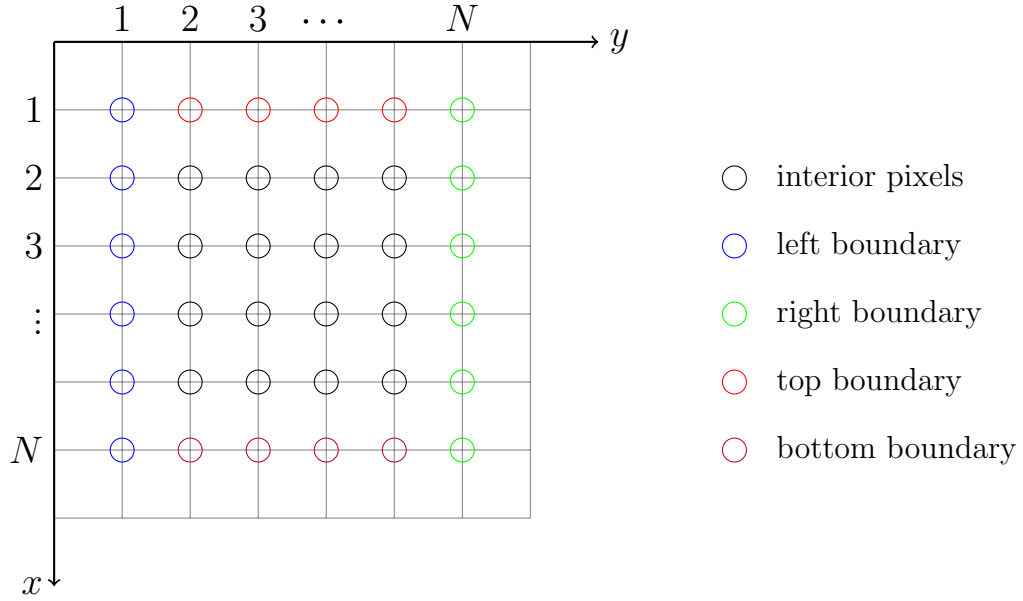


Figure 2.3: Pixel classification according to location within image: interior, or boundary. Corner pixel (1,1) belongs to top and left boundaries. The other corner pixels share a similar property.

Finally, the initial condition is discretized by

$$u_{ij}^0 = u_0(x_i, y_j). \tag{2.17}$$

2.4 Experiments

Using Matlab, we have written code to test the proposed model on a number of images. On each example the original image is shown along with the location (chosen arbitrarily) of the initial contour to be evolved. A more judicious selection of the initial curve is expected to translate in more accurate and faster segmentations. Via experimentation, we have settled on a standard set of parameters for its implementation. Unless stated otherwise, we choose $\alpha = 25$, the time step $\Delta t = 1$, the standard deviation $\sigma = 1$, and the length of the local neighborhood $\rho = 20$. We also present segmentation results using models proposed in [66], the *global* model, and in [57], the *local* model. We have chosen to compare our PDE-based model to

these because they are also PDE-, region-based but ours takes advantage of edge data.

Our first example features an image with a number of objects, an array of coins, to be detected. Both the global and proposed model render a correct segmentation whereas the local model suggests the presence of a band surrounding the coins (Fig. 2.4). Note that the original contour splits to locate all objects in the image, an advantage provided by the embedded level set method implementation.

In Fig. 2.5 the global model (which assumes piecewise constant regions in the image) fails to identify the silhouette of the plane that conspicuously stands out. The local and proposed models correctly identify the object of interest. Note further that the segmentation of our model converges closer to the boundaries of the plane. This particular experiment shows that the proposed model exhibits certain robustness over initialization as the initial front barely touches the target object.

Figure 2.6 shows the results of the models on an image with nonuniform background. In practice such backgrounds are regarded as being contaminated by noise; coarse segmentation is desired so that small variations in the background are ignored. In addition, pre-processing tasks as such image denoising are usually applied to the image prior to segmentation. Our proposed, as mentioned, does not exert control over the arc length of the moving front. Nevertheless, our model provides a much *cleaner* result disregarding almost all the irregularities of the background near the object of interest.

Finally, in Fig. 2.7, we test the algorithms on an MRI image of the brain. Such images contain smooth boundaries that are hard to detect by deformable models. Note that the proposed model provides a greater number of these features than the global and local models. In Chapter 4 we consider a more specific class of medical images where the models presented in this chapter and in Chapter 3 are applied to the detection of lesions from *dermoscopy* imagery.

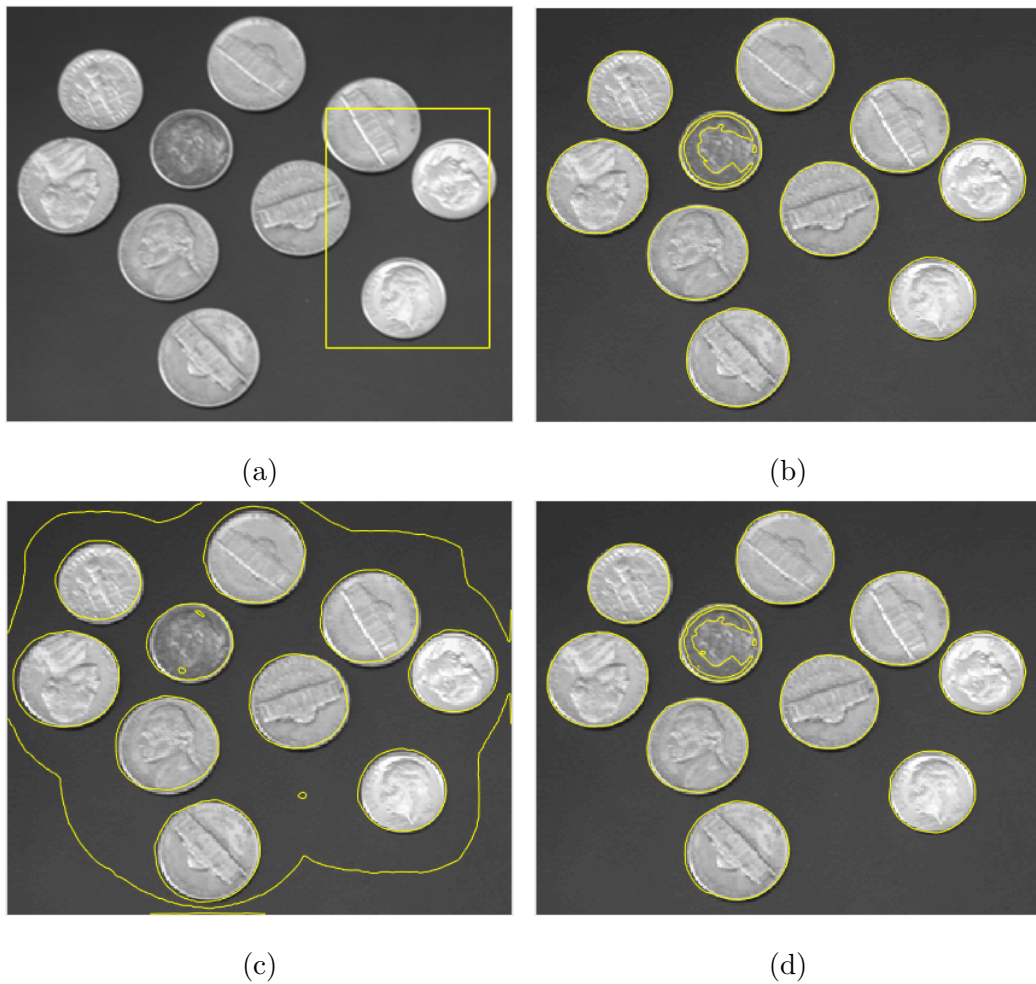


Figure 2.4: An image that poses a relatively simple segmentation problem. (a) Original image and initial contour, and final segmentations of (b) model proposed in [66], (c) model in [57], and (d) our proposed model.

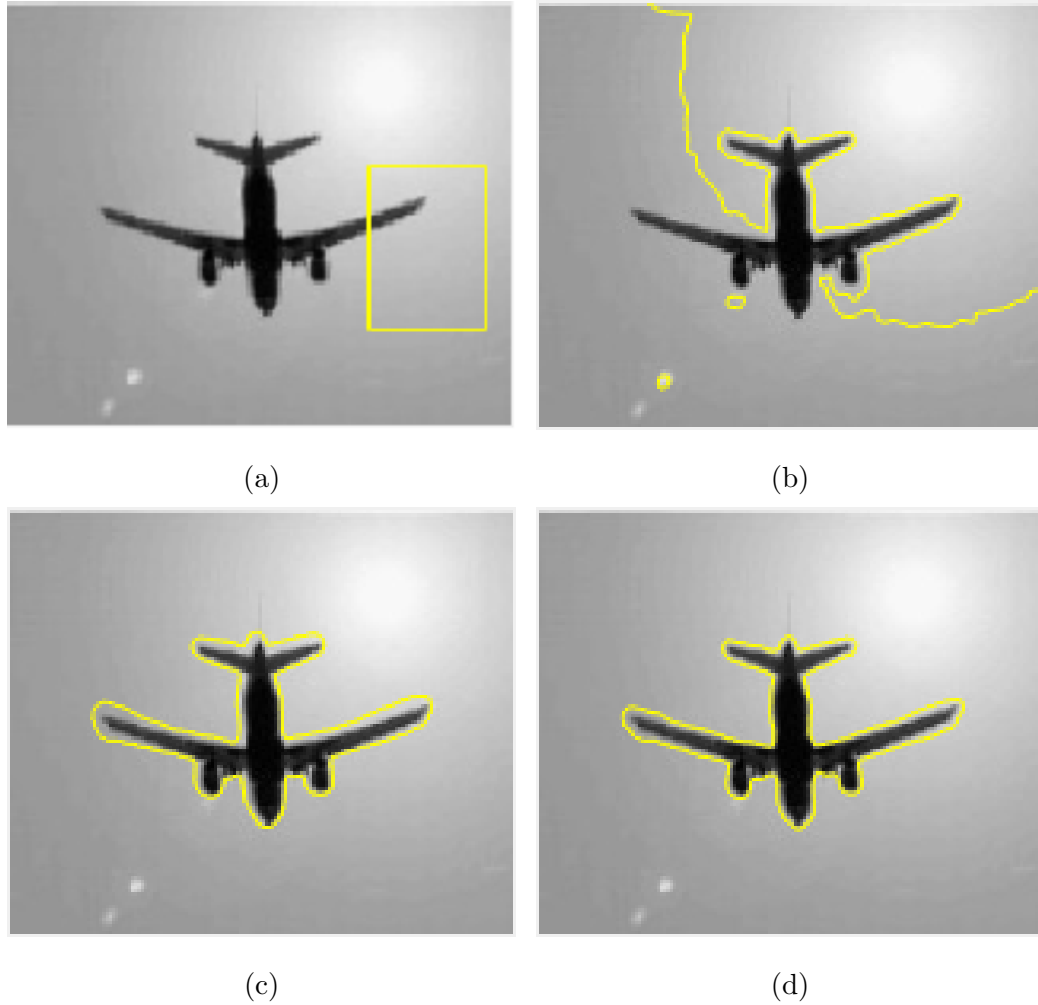


Figure 2.5: Robustness to initial condition: The global method in [66] fails to obtain a correct segmentation (a) Original image and initial contour, and final segmentations of (b) model proposed in [66], (c) model in [57], and (d) our proposed model.

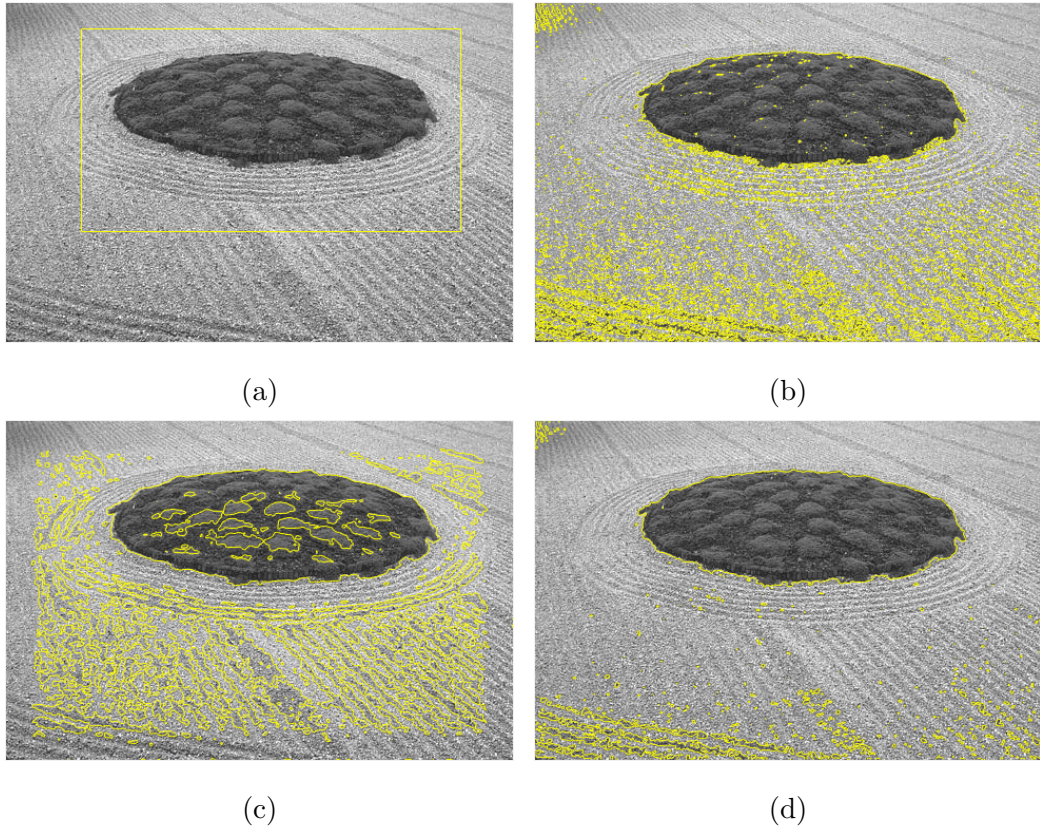


Figure 2.6: Sensitivity to noise and *noisy* features: Image with an irregular background that heavily hampers the segmentation results of [57, 66] on (b) and (c), respectively. Ours (d) is able to isolate the most meaningful object in the image. Parameters: $\alpha = 100$.

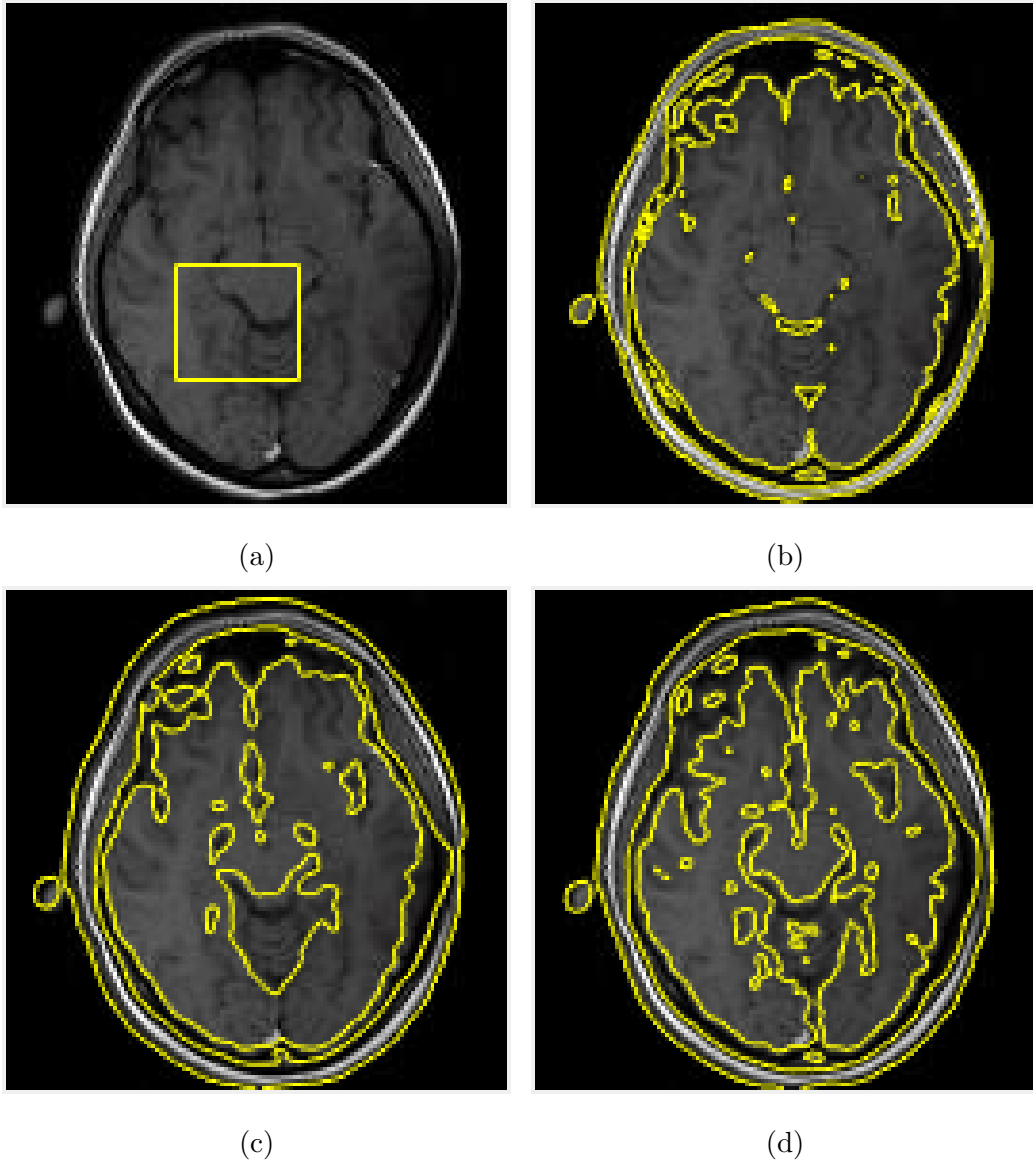


Figure 2.7: MRI image: The proposed model (d) captures the highest level of detail. (a) Original and initialization, (b) result using [66], (c) result using [57].

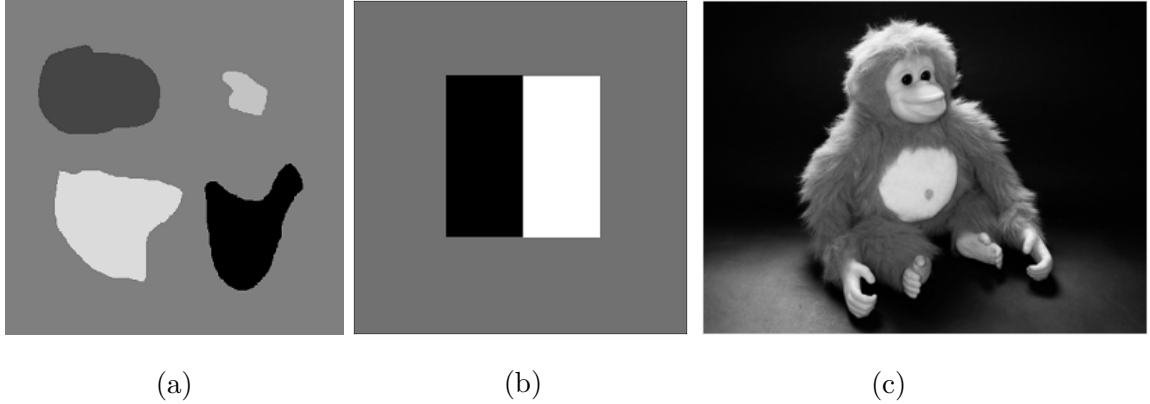


Figure 2.8: Representatives of three special classes of images. (a) Multimodal image; (b) image with triple junction of colors/graylevel; (c) image with nonuniform lighting.

2.5 Further Experiments

Many images consist of two distinguishable regions, background and foreground; this is the basic premise of our model. However, some images can have three or more objects of interest along with the background. For example, two objects of different color placed adjacent to each other on a tabletop. We refer to these images as *multimodal* images. Also, images with nonuniform lighting prove difficult to segment, Fig. 2.8. In this section we test our PDE-based model against representatives of these image classes to provide a proof of concept for the model we shall introduce in Chapter 3.

2.5.1 Performance on multimodal images

The first experiment attempts a segmentation of an multimodal image with four nonadjacent objects of different graylevel and background, as in Fig. 2.8a. The goal is to obtain a separation of the four objects. Perhaps traditional methods such as multithresholding [17] or region growing [26] are able to delineate every object in this image, but the task is not as straightforward for deformable models. In fact, our PDE-based model is only able to separate the object with highest contrast

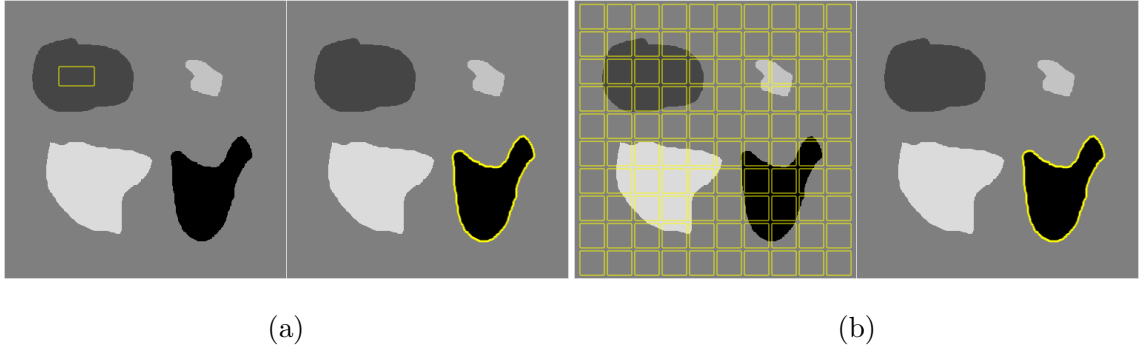


Figure 2.9: Unsuccessful segmentation of multimodal image. Our PDE-based model is only able to separate the object with highest contrast relative to the background regardless initialization. (a) and (b) show two initializations and their respective (identical) steady states.

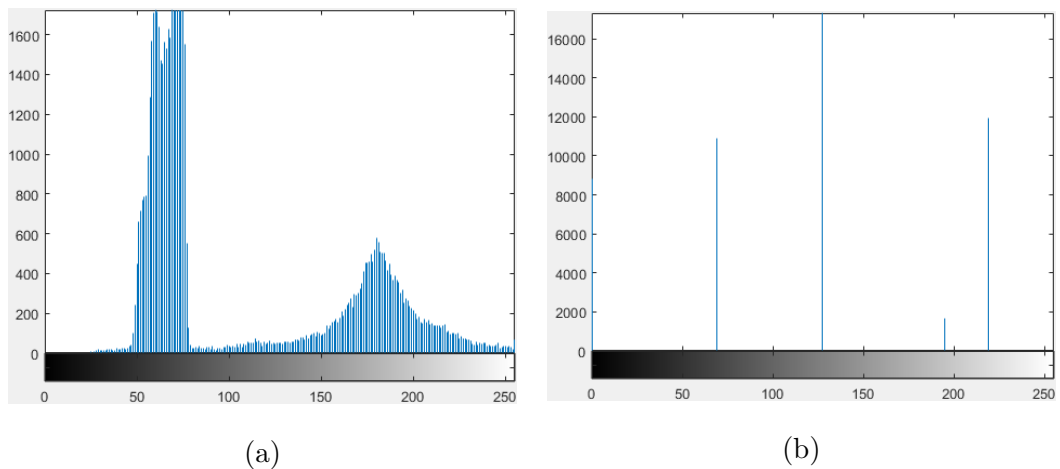


Figure 2.10: Graylevel histograms for (a) ‘coin’ and (b) ‘four-object’ images.

relative to the image background without performing pre-processing tasks such as histogram equalization or histogram matching [26], Fig. 2.9. It is interesting to compare this result with that of Fig. 2.4 in which all the objects (the coins, some of which have different graylevel intensities) in the scene were successfully detected by the model. Inspection of the image histograms reveals the reason why this occurs, Fig. 2.10. Our PDE-based model measures deviations of I from the intensity means inside and outside the evolving front as this moves about the image domain. Due to the jumps in the frequency distribution for the ‘four-object’ image and lack of continuity across the *dynamic range* of the image, the means (2.5) remain constant

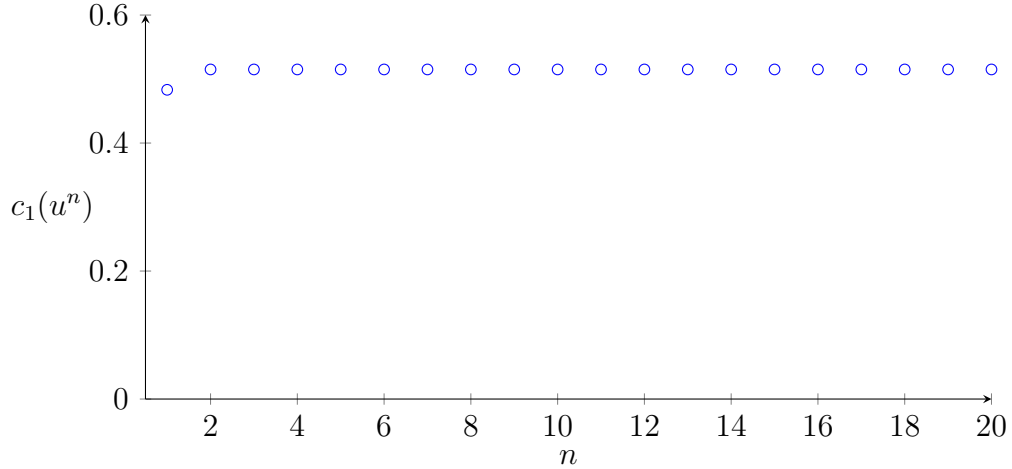
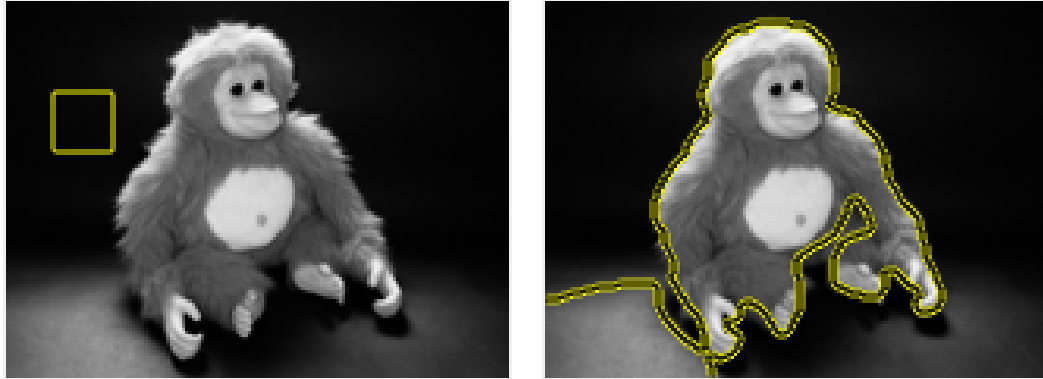


Figure 2.11: Intensity mean inside front c_1 as function of number of *iterations* for ‘four-object’ image.

for each iterative step n , making the evolving curve converge after just one iteration, Fig. 2.11. Therefore, only one object is detected by our model. For such images, and other *texture* images [65], graylevel information is inadequate. In Chapter 5 we discuss other image discriminants and techniques that could prove useful for object detection in multimodal imagery.

2.5.2 Images with Nonuniform Illumination

Shading (also intensity nonuniformity, intensity inhomogeneity, ect.) occurs often in everyday and specialized imagery [25]. This phenomenon may originate from imperfections of the image acquisition process or inadequate object preparation [35, 59]. Uniform lighting is desirable because pixels of the same class (within an object, for example) are expected to possess equal brightness (graylevel) regardless of their location within the image. Lack of uniform illumination in an image can hamper its viability for analysis; this is particularly true when using mathematical models for object detection. In particular, our PDE-based model, being a region based model that combines global and local statistics via edge data, is not impervious to



(a)

(b)

Figure 2.12: Segmentation of ‘monkey’ image by PDE-base model.(a) Original and initialization, (b) final segmentation. Bright region on the floor is also detected as a possible region of interest.

the negative effects of severe intensity inhomogeneity. Consider again the ‘monkey’ image from Fig. 2.8c. Note the regions that are very bright (head, hands, abdomen, face, and shoulders) within the monkey itself and the floor. Not only is illumination not uniform, the monkey itself is a multimodal object (belly, face, eyes, fur, etc.). Segmentation results for the PDE-based model are shown in Fig. 2.12

We will address these weaknesses, at least partially, in the next chapter where we propose our second model for image segmentation based on a variational formulation.

CHAPTER 3
A HYBRID VARIATIONAL MODEL FOR BOUNDARY DETECTION

In the previous chapter we presented a PDE-based hybrid model (combining both edge and region data) by directly specifying the evolution equation for an initial curve C_0 . One expects the steady state of the PDE to correspond (in principle) to the boundary of objects in an image. The formulation of the model relied on a number of assumptions which lead, in turn, to the formulation of speeds F that propagate points \mathbf{x} of C_0 toward the edges of relevant regions. In this chapter we propose a hybrid model for image segmentation based on a variational formulation. We draw inspiration from the models in references [7, 29, 64].

3.1 Preliminaries

Let the image domain $D \subset \mathbb{R}^2$ be open and bounded, and $I : D \rightarrow \mathbb{R}$ the given image. In [64] (see also [65]) it is assumed that I is *bimodal*, that is, it consists of two regions, foreground and background, with respective constant intensities ι_1, ι_2 , with $\iota_1 \neq \iota_2$ ¹. Let $C(\mathbf{x}, t) : D \times [0, \infty) \rightarrow \mathbb{R}^2$ be a family of planar curves in the image domain, and μ_1, μ_2 be, respectively, the mean intensity of I inside and outside $C(\cdot, t)$. Then

$$\mu_1 = \mu_1(\mathbf{x}, \Omega) = \frac{1}{|\Omega|} \int_{\Omega} I(\mathbf{x}) \, d\mathbf{x}, \tag{3.1a}$$

$$\mu_2 = \mu_2(\mathbf{x}, \Omega) = \frac{1}{|\Omega^c|} \int_{\Omega^c} I(\mathbf{x}) \, d\mathbf{x}, \tag{3.1b}$$

¹We will relax this condition later.

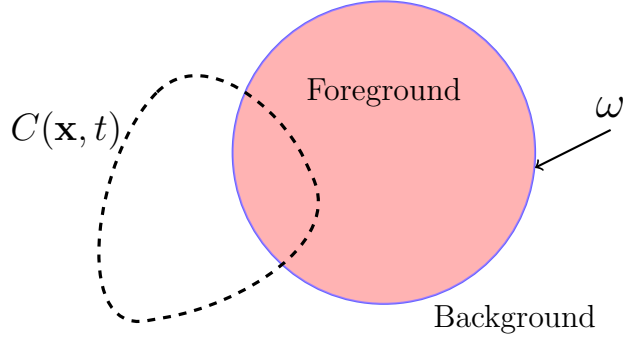


Figure 3.1: Composition of a bimodal image. Foreground (in color), background, and the boundary ω (in blue) separating the two regions. A segmentation is obtained as C approaches ω .

$$|\Omega| = \int_{\Omega} d\mathbf{x}, \quad (3.2)$$

where Ω is the interior of $C(\cdot, t)$, and Ω^c its exterior. Let ω represent the *ideal* boundary separating the background and foreground regions in I (see Fig. 3.1). Clearly, as C approaches the unknown boundary ω the absolute difference of the dynamic means μ_1, μ_2 increases and gets closer to the absolute difference of the region intensities ι_1, ι_2 . In symbols,

$$|\mu_1 - \mu_2| \rightarrow |\iota_1 - \iota_2| \text{ as } C \rightarrow \omega. \quad (3.3)$$

In this way, C gives a *separation* of the foreground and background regions according to the “distance” separating their respective means. Based on this analysis, the following variational formulation is proposed [64]:

$$\sup E = \sup (\mu_1 - \mu_2)^2, \quad (3.4)$$

where the sup is taken over all admissible deformations of the curve C on $W^{1,2}(D) = \{C \in L^2(D); \nabla C \in L^2(D)\}$. We call this model the Mean Separation (MS) model as in [31]. When the images are not bimodal, however, the model (3.4) is not effective for segmentation of more general images, Fig. 3.2.



Figure 3.2: Incorrect segmentation using separation of means. (a) Original image and initial curve, and (b) final segmentation. The evolving curve is attracted to the brightest regions in the image.

3.2 Model Formulation

To extend the capabilities of model (3.4) to a larger class of images we reformulate it as a minimization problem. Further, we incorporate an edge function g (as in (1.31), for example) to augment its scope for boundary detection. We thus propose the following energy for object detection:

$$\hat{E}(\mathbf{x}, \Omega) = -\frac{1}{2}g(\mathbf{x})(\mu_1 - \mu_2)^2 \quad (3.5)$$

where μ_1, μ_2 are as in equations (3.1a) and (3.1b). Minima of (3.5) (possibly local) are expected to attract evolving curves toward object boundaries due to forces exerted by the region features embedded in the *separation* of the means μ_1, μ_2 , while the edge function g pins down the contours to salient discontinuities. To further strengthen (3.5) we add a regularization term [58]

$$L = \oint_C ds \quad (3.6)$$

which penalizes C to have minimal arc length. We do so via a Lagrange multiplier $\lambda > 0$ which controls the influence of the regularizing effects of (3.6). The resulting

model is

$$E(\mathbf{x}, \Omega) = -\frac{1}{2} g(\mathbf{x}) (\mu_1 - \mu_2)^2 + \lambda \oint_{\partial\Omega} ds. \quad (3.7)$$

We pause for a moment to put matters in mathematical perspective. While the energies for the variational models presented in Chapter 1 involved line (boundary) integrals, energy (3.7) not only entails such integrals (regularization term), it also involves region integrals. As a result, the techniques presented in Chapter 1 do not apply (at least directly) to model (3.7). In particular, the first term in (3.7) requires special treatment. We address how to obtain the Gateaux derivatives of region functionals in the next section. This will lead to the associated Euler equations, which in turn lead to the evolution parabolic PDE for our proposed model.

3.3 Velocity Fields of Region Functionals

As we showed in the introduction of this thesis, solutions of variational problems typically involve PDEs (Euler equations) whose solution determines minima of the associated energies. If the energy involves only line integrals, the techniques of Chapter 1 are sufficient to compute the velocity fields. Energies like the one we propose in the previous section involve region functionals. To handle these, two approaches are possible:

- a) either, as it is classical, the region integrals are converted to line integrals, which is possible by invoking solutions of Poisson's equation with Dirichlet conditions and an application of Green's theorem, or
- b) obtain the Euler equations from the region functionals directly using *shape derivation* methods.

We choose the former approach and remark that the latter has interest in its own right. We refer the reader to [5] and references therein for more on shape derivation.

3.3.1 Converting Region Integrals to Boundary integrals

We follow [5]. Let us consider region integrals of the form

$$F(\Omega) = \int_{\Omega} f(\mathbf{x}, \Omega) d\mathbf{x} \quad (3.8)$$

where f is a scalar function and Ω is an open, regular and bounded subset of \mathbb{R}^n with boundary $\partial\Omega$. We prove the following result.

PROPOSITION 3.1. *Let Ω be a bounded open set with regular boundary $\partial\Omega$. Let $f : \bar{\Omega} \rightarrow \mathbb{R}$ be continuous and u the unique solution of Poisson's equation:*

$$\begin{cases} -\Delta u = f & \text{in } \Omega, \\ u = 0 & \text{on } \partial\Omega. \end{cases} \quad (3.9)$$

The following identity holds:

$$\int_{\Omega} f(\mathbf{x}, \Omega) d\mathbf{x} = \int_{\partial\Omega} \nabla u \cdot \vec{\mathcal{N}} ds. \quad (3.10)$$

Proof. Let u satisfy the hypothesis. Then,

$$\int_{\Omega} f(\mathbf{x}, \Omega) d\mathbf{x} = - \int_{\Omega} \Delta u d\mathbf{x} = \int_{\partial\Omega} \nabla u \cdot \vec{\mathcal{N}} ds.$$

The first equality follows by (3.9) inside Ω , and the second by Green's theorem. The proof is complete.

3.3.2 Computation of the Gateaux derivative

With the region integrals converted into line integrals, we can follow the ideas of Chapter 1 to obtain the Euler equation associated with energy (3.7). But first we obtain the general result for functional (3.8).

THEOREM 3.2. *The Gateaux derivative of (3.8) is*

$$F'(\Omega) = - \int_0^1 C_t \cdot f \vec{\mathcal{N}} ds = - \int_0^1 C_t(q) \cdot f(C(q)) \vec{\mathcal{N}} ds.$$

Note that F' does not depend on u , but on the original integrand of functional (3.8).

Proof. By Proposition 3.1 we have

$$\int_{\Omega} f(\mathbf{x}, \Omega) d\mathbf{x} = \int_{\partial\Omega} \nabla u \cdot \vec{\mathcal{N}} ds. \quad (3.11)$$

Explicitly the gradient (column) vector² field of u is

$$\nabla u = \langle u_x, u_y \rangle^T, \quad (3.12)$$

and the inward unit normal vector $\vec{\mathcal{N}}$ to $\partial\Omega$ is

$$\vec{\mathcal{N}} = \frac{\langle -y_q, x_q \rangle^T}{\|C_q\|}. \quad (3.13)$$

Note that we could use the *principal* unit normal vector as in (1.15) but the above representation is simpler. Substituting (3.12) and (3.13) in (3.11) we get

$$\int_{\Omega} f(\mathbf{x}, \Omega) d\mathbf{x} = \int_{\partial\Omega} \nabla u \cdot \vec{\mathcal{N}} dq = \int_0^1 (u_y x_q - u_x y_q) dq. \quad (3.14)$$

Differentiating with respect to t gives

$$\begin{aligned} F'(\Omega) &= \frac{d}{dt} F(\Omega) = \int_0^1 \frac{d}{dt} (u_y x_q - u_x y_q) dq \\ &= \int_0^1 (x_q \nabla u_y \cdot C_t + u_y x_{qt} - (y_q \nabla u_x \cdot C_t + u_x y_{qt})) dq \\ &= \int_0^1 ((x_q \nabla u_y - y_q \nabla u_x) \cdot C_t + \langle u_y, -u_x \rangle \cdot C_{qt}) dq. \end{aligned} \quad (3.15)$$

Integrating the second term of the last equation above by parts, one has

$$\begin{aligned} F'(\Omega) &= \int_0^1 (x_q \nabla u_y - y_q \nabla u_x - \langle \nabla u_y \cdot C_q, -\nabla u_x \cdot C_q \rangle^T) \cdot C_t dq \\ &= \int_0^1 ((u_{xx} + u_{yy}) \langle -y_q, x_q \rangle^T) \cdot C_t dq \\ &= \int_0^1 (\Delta u \vec{\mathcal{N}} \|C_q\|) \cdot C_t dq. \end{aligned} \quad (3.16)$$

The hypothesis of Proposition 3.1, $\Delta u = -f$, and the fact that $ds = \|C_q\|dq$ verifies the claim. The proof is complete.

²We use $\vec{V}^T = \langle a, b \rangle^T$ to denote the transpose of the row vector \vec{V} .

We now compute the Gateaux derivative of energy (3.7). Its first term is the region functional to which Theorem 3.2 applies. The derivative of the second term was obtained in equation (1.19) of Section 1.2.1:

$$L'(t) = - \int_0^{L(t)} C_t \cdot \kappa \vec{N} ds, \quad (3.17)$$

where κ is the mean curvature of at each pixel \mathbf{x} of C . Consider now the region dependent term of (3.7):

$$R(\mathbf{x}, \Omega) = -\frac{1}{2} g(\mathbf{x}) (\mu_1 - \mu_2)^2, \quad (3.18)$$

where the region functionals are embedded in the means μ_1, μ_2 (equation (3.1)). The Gateaux derivative of (3.18) is

$$\begin{aligned} R'(\mathbf{x}, \Omega) &= -\frac{1}{2} g(\mathbf{x}) \frac{d}{dt} (\mu_1 - \mu_2)^2 \\ &= g(\mathbf{x}) (\mu_2 - \mu_1) \frac{d}{dt} (\mu_1 - \mu_2) \\ &= g(\mathbf{x}) (\mu_2 - \mu_1) \left(\frac{d}{dt} \mu_1 - \frac{d}{dt} \mu_2 \right) \end{aligned} \quad (3.19)$$

where we have used the chain rule and the fact that $g = g(I(\mathbf{x}))$ does not change with time. The problem has been reduced to computing the derivatives of μ_1 and μ_2 . We consider each individually beginning with μ_1 :

$$\begin{aligned} \frac{d}{dt} \mu_1 &= \frac{d}{dt} \left(\frac{\int_{\Omega} I d\mathbf{x}}{\int_{\Omega} d\mathbf{x}} \right) \\ &= \frac{\int_{\Omega} d\mathbf{x} \frac{d}{dt} (\int_{\Omega} I d\mathbf{x}) - \frac{d}{dt} (\int_{\Omega} d\mathbf{x}) \int_{\Omega} I d\mathbf{x}}{(\int_{\Omega} d\mathbf{x})^2}. \end{aligned} \quad (3.20)$$

By Theorem 3.2, $\frac{d}{dt} (\int_{\Omega} I d\mathbf{x}) = - \int_0^1 C_t \cdot I \vec{N} ds$ and $\frac{d}{dt} (\int_{\Omega} d\mathbf{x}) = - \int_0^1 C_t \cdot \vec{N} ds$. Also, to simplify notation, we write $|\Omega|$ for $\int_{\Omega} d\mathbf{x}$. Substituting these expressions in (3.20)

we get

$$\begin{aligned}
\frac{d}{dt}\mu_1 &= \frac{\int_0^1 C_t \cdot \vec{\mathcal{N}} ds \int_{\Omega} I d\mathbf{x} - |\Omega| \int_0^1 C_t \cdot I \vec{\mathcal{N}} ds}{|\Omega|^2} \\
&= \frac{\int_0^1 C_t \cdot \mu_1 \vec{\mathcal{N}} ds - \int_0^1 C_t \cdot I \vec{\mathcal{N}} ds}{|\Omega|} \\
&= - \frac{\int_0^1 C_t \cdot (I - \mu_1) \vec{\mathcal{N}} ds}{|\Omega|} \\
&= - \int_0^1 C_t \cdot \frac{I - \mu_1}{|\Omega|} \vec{\mathcal{N}} ds
\end{aligned} \tag{3.21}$$

For $\mu_2 = \int_{\Omega^c} I d\mathbf{x} / \int_{\Omega^c} d\mathbf{x}$, we note that the inner normal vector to Ω^c is $-\vec{\mathcal{N}}$. Its Gateaux derivative is computed in similar fashion:

$$\frac{d}{dt}\mu_2 = \int_0^1 C_t \cdot \frac{I - \mu_2}{|\Omega^c|} \vec{\mathcal{N}} ds. \tag{3.22}$$

Finally, using (3.21) and (3.22) in (3.19) results after some rearranging in:

$$R'(\mathbf{x}, \Omega) = - \int_0^1 C_t \cdot g(\mathbf{x})(\mu_2 - \mu_1) \left(\frac{I - \mu_1}{|\Omega|} + \frac{I - \mu_2}{|\Omega^c|} \right) \vec{\mathcal{N}} ds, \tag{3.23}$$

and adding (3.17) and (3.23) we arrive at the Gateaux derivative for the proposed model:

$$E'(\mathbf{x}, \Omega) = - \int_0^1 C_t \cdot \left[g(\mathbf{x})(\mu_2 - \mu_1) \left(\frac{I - \mu_1}{|\Omega|} + \frac{I - \mu_2}{|\Omega^c|} \right) + \lambda\kappa \right] \vec{\mathcal{N}} ds. \tag{3.24}$$

3.3.3 Construction of the velocity field for the solution of $\min E$

From the Gateaux derivative we immediately obtain the associated Euler equation. Starting from an initial curve $C(\mathbf{x}, 0) = C_0$ the steepest descent method gives the following evolution equation the minima of (3.7):

$$C_t = g(\mathbf{x})(\mu_2 - \mu_1) \left(\frac{I - \mu_1}{|\Omega|} + \frac{I - \mu_2}{|\Omega^c|} \right) \vec{\mathcal{N}} + \lambda\kappa \vec{\mathcal{N}}. \tag{3.25}$$

We expect the steady state of (3.25) to provide meaningful image partitions taking advantage of both edge and statistical information from more general images.

3.4 Numerical Implementation

Again, we use the level set method for the numerical implementation of (3.25). Let C be represented by the zero levels set of the embedding curve $u : \mathbb{R}^2 \rightarrow \mathbb{R}$. Then (see Section 1.2.3):

$$\nabla u \cdot C_t + u_t = 0 \quad (3.26)$$

Using (3.25) in (3.26) along with $\vec{\mathcal{N}} = -\nabla u / \|\nabla u\|$ we obtain the evolution of C in terms of the level sets of u :

$$\begin{aligned} u_t &= -\nabla u \cdot C_t \\ &= \nabla u \cdot \left(g(\mathbf{x})(\mu_2 - \mu_1) \left(\frac{I - \mu_1}{|\Omega|} + \frac{I - \mu_2}{|\Omega^c|} \right) + \lambda \kappa \right) \frac{\nabla u}{\|\nabla u\|} \\ &= \left(g(\mathbf{x})(\mu_2 - \mu_1) \left(\frac{I - \mu_1}{|\Omega|} + \frac{I - \mu_2}{|\Omega^c|} \right) + \lambda \kappa \right) \|\nabla u\|. \end{aligned}$$

In terms of u the curvature $\kappa = \operatorname{div}(\nabla u / \|\nabla u\|)$. Using this in the above equation we arrive at the level set evolution model for the solution of problem (3.7):

$$\begin{cases} u_t = \left[g(\mathbf{x})(\mu_2 - \mu_1) \left(\frac{I - \mu_1}{|\Omega|} + \frac{I - \mu_2}{|\Omega^c|} \right) + \lambda \operatorname{div} \left(\frac{\nabla u}{\|\nabla u\|} \right) \right] \|\nabla u\| \\ \frac{\partial u}{\partial \vec{n}} = 0 \text{ on } \partial\Omega \quad (\text{Neumann boundary condition}) \\ u(\mathbf{x}, 0) = u_0(\mathbf{x}) \quad (\text{initial condition}) \end{cases} \quad (3.27)$$

Equation (3.27) gives the evolution of all the levels sets of u . However, we are only interested in the zero level set which represents C_t . For our purposes it is sufficient to only consider pixels \mathbf{x} in a small neighborhood (strip or band) of the zero level set. Aiming for computational efficiency, we implement localized techniques known as *narrowband methods*. We refer the interested reader to references [1, 51, 52] for details. For the discretization of (3.27) we employ forward differences for the time derivatives and central differences for the spacial derivatives at interior pixels and forward/backward differences for pixels at the boundary, as we did in Section 2.3

for our PDE-based model, and hence we will not repeat this analysis. We only detail how to obtain the curvature κ as it involves second partial derivatives. By definition,

$$\kappa = \operatorname{div} \left(\frac{\nabla u}{\|\nabla u\|} \right)$$

and expanding the divergence operator gives

$$\begin{aligned} \kappa &= \operatorname{div} \left(\frac{\nabla u}{\|\nabla u\|} \right) \\ &= \frac{\partial}{\partial x} \left(\frac{u_x}{(u_x^2 + u_y^2)^{1/2}} \right) + \frac{\partial}{\partial y} \left(\frac{u_y}{(u_x^2 + u_y^2)^{1/2}} \right). \end{aligned}$$

After using the quotient rule and some simplification we obtain

$$\kappa = \frac{u_{xx}u_y^2 - 2u_{xy}u_xu_y + u_{yy}u_x^2}{(u_x^2 + u_y^2)^{3/2}}. \quad (3.28)$$

Clearly, approximations to the second order partial derivatives u_{xx} , u_{yy} , and u_{xy} are needed for the approximation of κ . Let h represent the spatial step size on either direction. From Taylor's theorem we have the following expansions:

$$u(x+h, y) = u(x, y) + hu_x(x, y) + \frac{h^2u_{xx}(x, y)}{2} + \frac{h^3u_{xxx}(x, y)}{6} + O(h^4) \quad (3.29)$$

$$u(x-h, y) = u(x, y) - hu_x(x, y) + \frac{h^2u_{xx}(x, y)}{2} - \frac{h^3u_{xxx}(x, y)}{6} + O(h^4) \quad (3.30)$$

Adding (3.29) and (3.29) yields

$$u(x+h, y) + u(x-h, y) = 2u(x, y) + h^2u_{xx}(x, y) + O(h^4) \quad (3.31)$$

and solving for u_{xx} gives the second order accurate formula

$$u_{xx}(x, y) \approx \frac{u(x+h, y) - 2u(x, y) + u(x-h, y)}{h^2}. \quad (3.32)$$

which can be written using subindex notation as

$$u_{xx}|_{ij}^n \approx \frac{u_{i+1,j}^n - 2u_{ij}^n + u_{i-,j}^n}{h^2} \quad (3.33)$$

for every iteration n and interior pixel $(ih, jh) = (i, j)$. Similarly for u_{yy} we get

$$u_{yy}|_{ij}^n \approx \frac{u_{i,j+1}^n - 2u_{ij}^n + u_{i,j-1}^n}{h^2}. \quad (3.34)$$

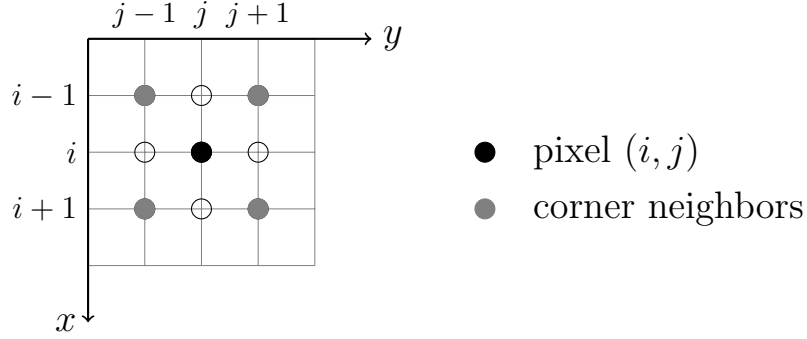


Figure 3.3: 3×3 neighborhood of pixel (i, j) . Corner neighbors are used for approximating mixed second order derivatives.

The second order mixed partial derivative u_{xy} requires more work. Refer to Fig. 3.3. At the four “corner” neighbors $u(x+h, y+h)$, $u(x-h, y-h)$, $u(x-h, y+h)$, and $u(x+h, y-h)$ we have the following expansions:

$$\begin{aligned}
 -u(x+h, y+h) &= -(u(x, y) + h(u_x(x, y) + u_y(x, y)) \\
 &\quad + \frac{h^2(u_{xx}(x, y) + u_{yy}(x, y))}{2} + h^2 u_{xy}(x, y)) + \dots
 \end{aligned} \tag{3.35}$$

$$\begin{aligned}
 -u(x-h, y-h) &= -(u(x, y) - h(u_x(x, y) + u_y(x, y)) \\
 &\quad + \frac{h^2(u_{xx}(x, y) + u_{yy}(x, y))}{2} + h^2 u_{xy}(x, y)) + \dots
 \end{aligned} \tag{3.36}$$

$$\begin{aligned}
 u(x+h, y-h) &= u(x, y) + h(u_x(x, y) - u_y(x, y)) \\
 &\quad + \frac{h^2(u_{xx}(x, y) + u_{yy}(x, y))}{2} - h^2 u_{xy}(x, y) + \dots
 \end{aligned} \tag{3.37}$$

$$\begin{aligned}
 u(x-h, y+h) &= u(x, y) - h(u_x(x, y) - u_y(x, y)) \\
 &\quad + \frac{h^2(u_{xx}(x, y) + u_{yy}(x, y))}{2} - h^2 u_{xy}(x, y) + \dots
 \end{aligned} \tag{3.38}$$

Adding equations (3.35) – (3.38) and solving for u_{xy} yields the fourth order accurate formula

$$u_{xy} = \frac{u(x+h, y+h) + u(x-h, y-h) - u(x+h, y-h) - u(x-h, y+h)}{4h^2}$$

or more concisely using subindex notation

$$u_{xy}|_{ij}^n = \frac{u_{i+1, j+1} + u_{i-1, j-1} - u_{i+1, j-1} - u_{i-1, j+1}}{4h^2}. \tag{3.39}$$

3.5 Simulations

To assess the strengths and weaknesses of our variational model, which we call the *Edge-Mean Separation* (EMS) model, in this section we demonstrate its performance on a number of images. In Section 3.5.1 the examples illustrate how the EMS model is able to process images that MS model is not able to segment. Other technical aspects are tested in Section 3.6.

3.5.1 Application to Wider Class of Images

We consider the ‘monkey’ image for our first example. We noted (Section 3.1) that the MS Model cannot delineate the boundaries of the relevant object for this image due to the presence of nonuniform lighting and bright regions within the object of interest. In Fig. 3.4, using the same initial curve as for the MS model, we obtain a meaningful segmentation of the monkey. Clearly, this example illustrates a significant improvement.

For our next experiment we consider a galaxy image. Figure 3.5 on p. 48 shows an example of a *spiral* galaxy with two spiral arms [16]. Our model is able to detect the “cognitive” boundary of this galaxy. Note further the presence of a large star at the end of the spiral arm extending toward the top of the image. Our model suggests the presence of a potential object of interest there along with nearby cosmic dust, gas, and other smaller stars—perhaps a second *bulge* [16].

Our third and final example shows a medical image involving two cells, Fig. 3.6, p. 48. The advantages of using a level set formulation are apparent: starting from a rectangular front, a change in topology occurs and the front adjust to the shape suggested by image’s objects of interest. As in the previous examples our proposed model provides the most meaningful segmentation.

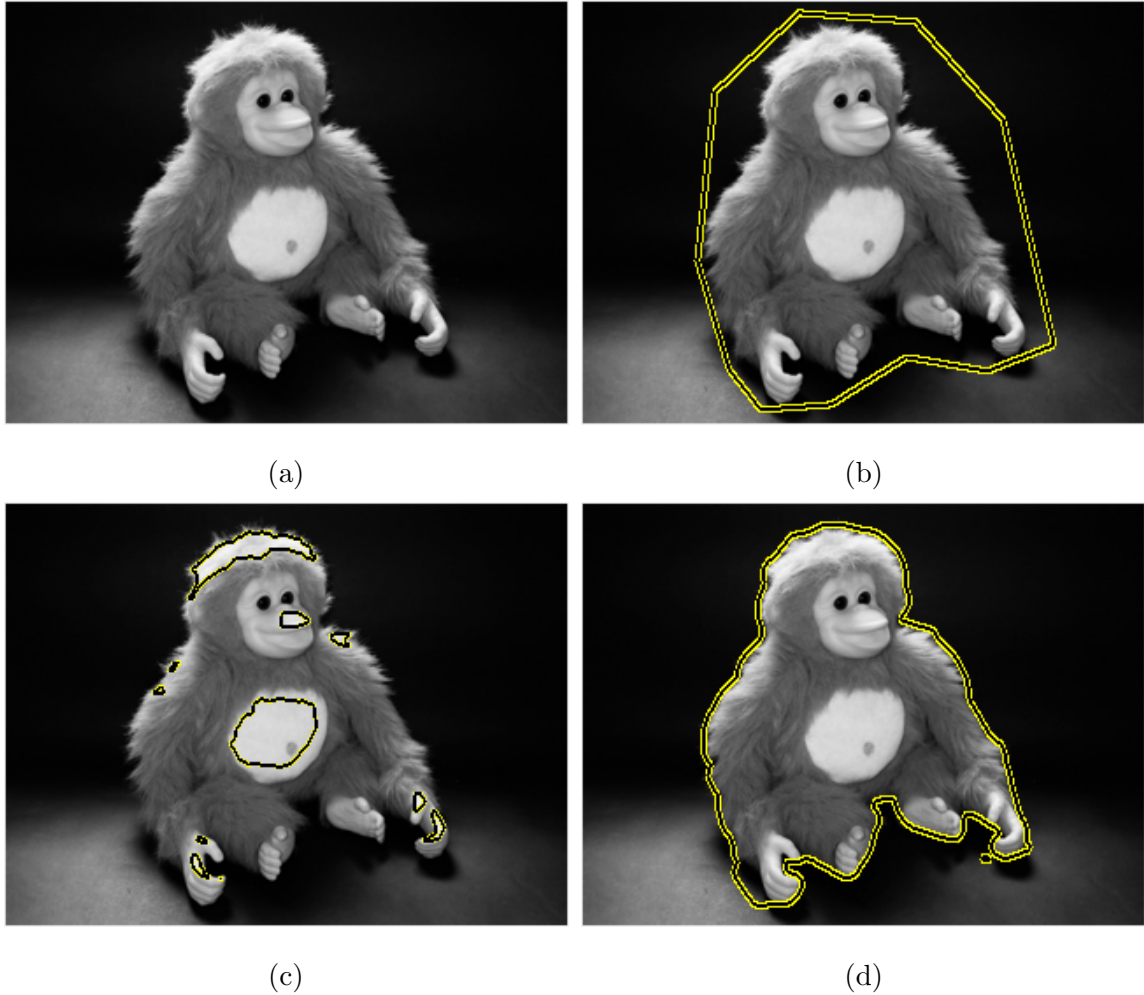


Figure 3.4: Successful segmentation using our proposed model. (a) Original image and (b) initial curve; (c) results with the MS model and (d) the proposed EMS model. The evolving curve clings to the outer edges of the monkey.

3.6 Further Experiments

In this section we show the results of several experiments we conducted to assess other properties that are desired of segmentation techniques. Sensitivity to initialization, performance on *multimodal* images, and sensitivity to noise are investigated.

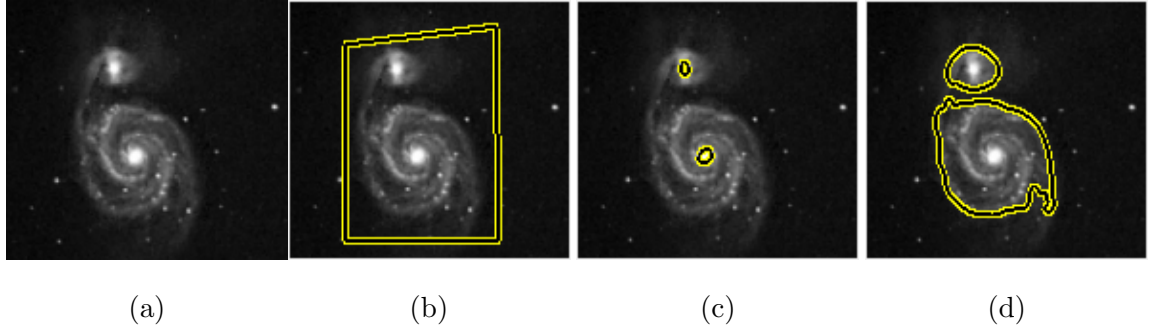


Figure 3.5: A successful segmentation of ‘galaxy’ image by our proposed model. (a) Original image and (b) initial curve; (c) results with the MS model and (d) the proposed EMS model. The “cognitive” boundary of the galaxy is suggested by our model.

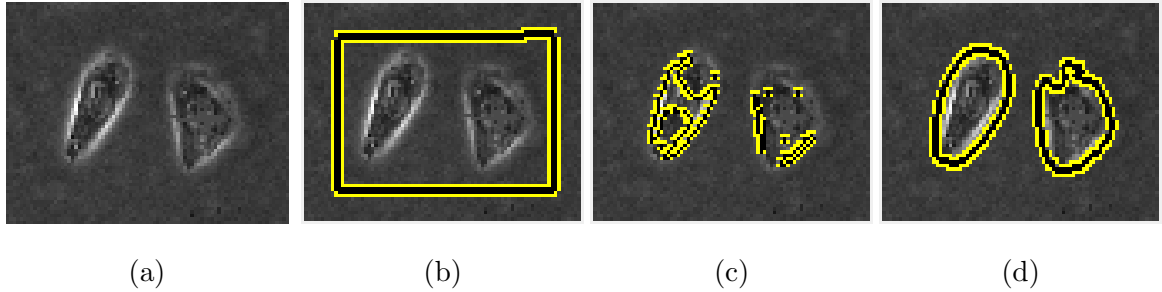


Figure 3.6: (a) Original image and (b) initial curve; (c) results with the MS model and (d) the proposed EMS model. The two cells are successfully detected by our model.

3.6.1 Sensitivity to Initialization

The problem of image segmentation from a PDE-Variational point of view is ill-posed. Although objects in images do not change (in some sense, they are unique) regardless of the location chosen for the initial evolving curves, two starting fronts $u_0, v_0, u_0 \neq v_0$, often render different solutions. Hence, there seems to be an unclear link between the steady state of evolution equations or (local) minima of energies and the particular image being segmented. Our proposed model does not escape this phenomenon. We tested our model against the ‘two cells’ image using a number of different initializations keeping all other parameters constant. Figure 3.7 shows eight different initializations. It is found that the model tends to yield meaningful

segmentations when single, regular initial curves surround the target objects. Also worth noting are initial curves shown in Fig. 3.7h. Contours of this form are desirable when detection of many objects is sought after. In this particular instance, not only the two cells were detected but also some structures within the left cell are suggested by the model as potential objects of interest.

3.6.2 Performance on multimodal images

In section Section 2.5 multimodal images were introduced. These images contain more than one region of interest (ROI) with different color/graylevel intensity. We also described the challenges they pose to PDE-based models. In this section we test our variational model on these images and discuss possible improvements.

Figure 3.8 shows our first experiment. The image consist of a square split into two black and white rectangles and the gray background. The three regions are adjacent to each other, a configuration commonly referred to as a *triple junction*. One could be interested in separating the square from the background or either rectangle. Starting from a front surrounding the target objects, our model is able detect the boundary of the square. This is possible due to incorporation of edge information. Region information alone fails as the gray level averages inside and outside the initial front are approximately equal (see Section 2.5.1). The model is able to detect either rectangle as well, starting from an overlapping front mostly contained within the target rectangle (Fig. 3.9).

Even if the objects of interest are not adjacent as in the example above, our model is still able to separate each object from the background, although selectively, Fig. 3.10. The model fails if no prior information is available and an unknown number objects are to be detected simultaneously with one single front.

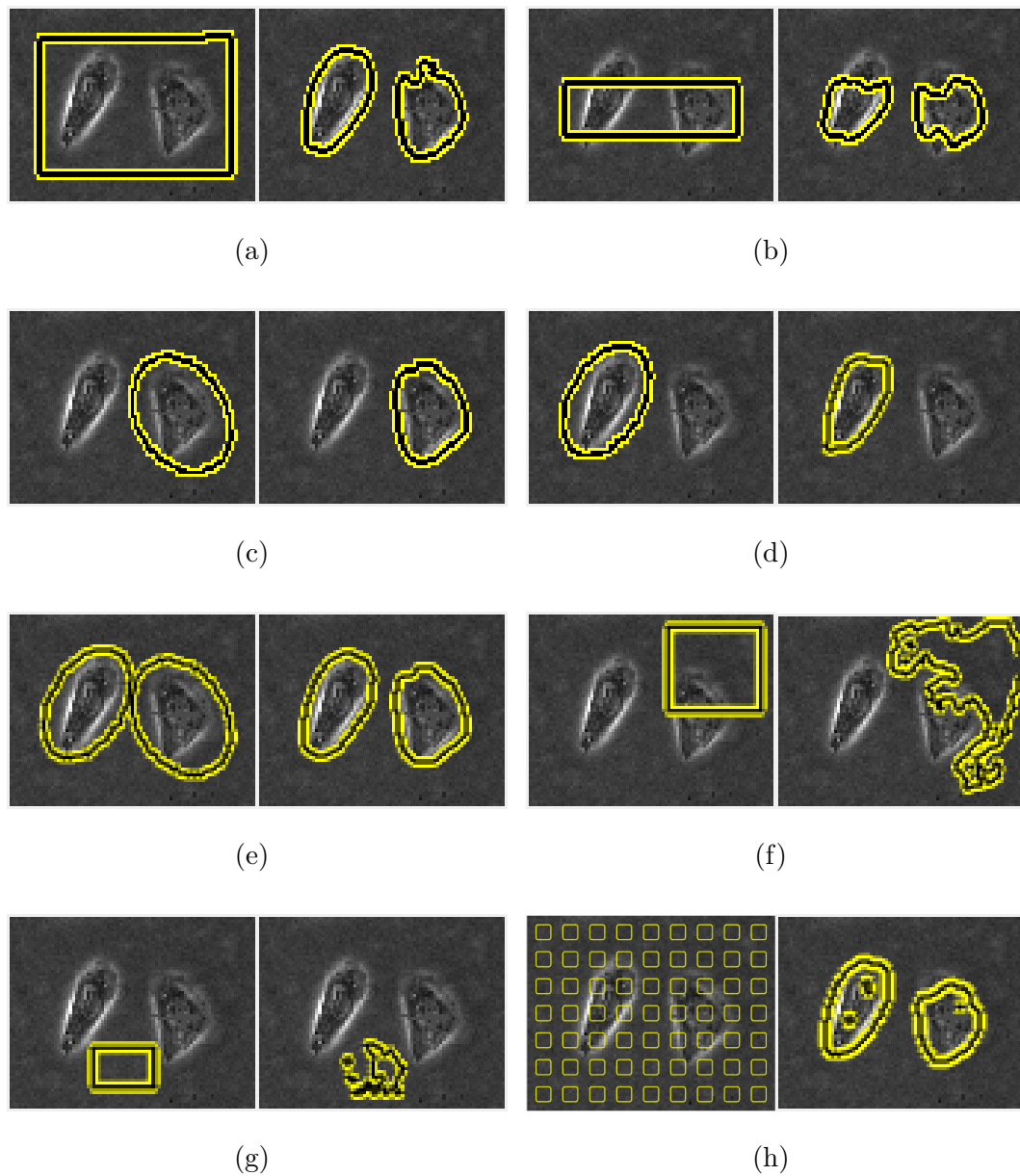


Figure 3.7: Sensible initializations of the evolving front plays a crucial role in the segmentation results for the proposed model. When initial contours encompass the target objects, as in (a) and (e), meaningful results are obtained. In (h) an almost correct segmentation is obtained if the detected region inside the cell on the left is neglected.

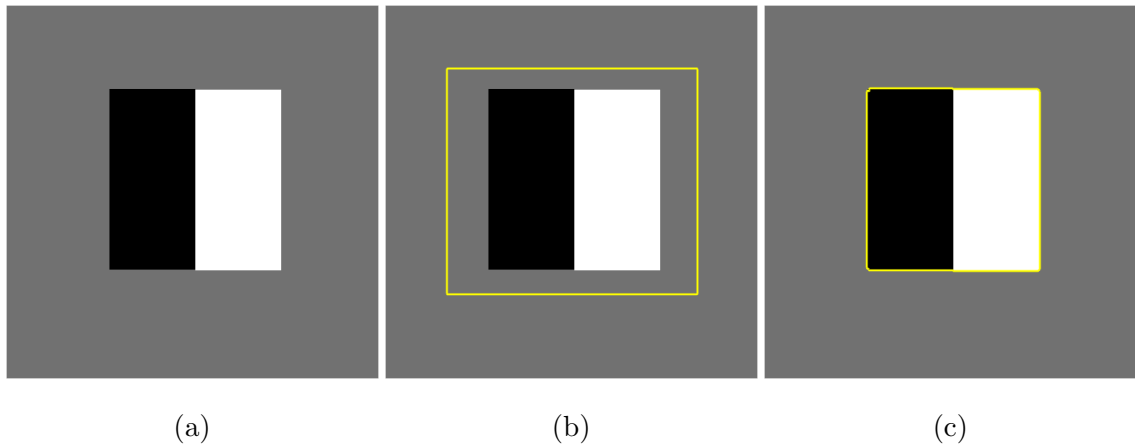


Figure 3.8: Segmentation of trimodal image with triple junction. (a) Original image and (b) initial curve; (c) result by proposed model. Boundaries of the outer square are detected.

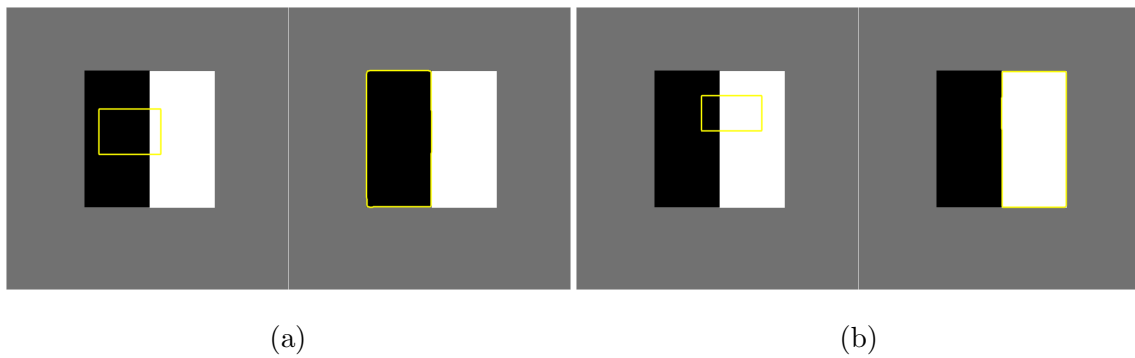


Figure 3.9: Selective segmentation in trimodal image with triple junction. Individual detection of (a) black and (b) white rectangle.



Figure 3.10: (a) Selective detection is still possible, (b) but detection of all objects in the scene is not.

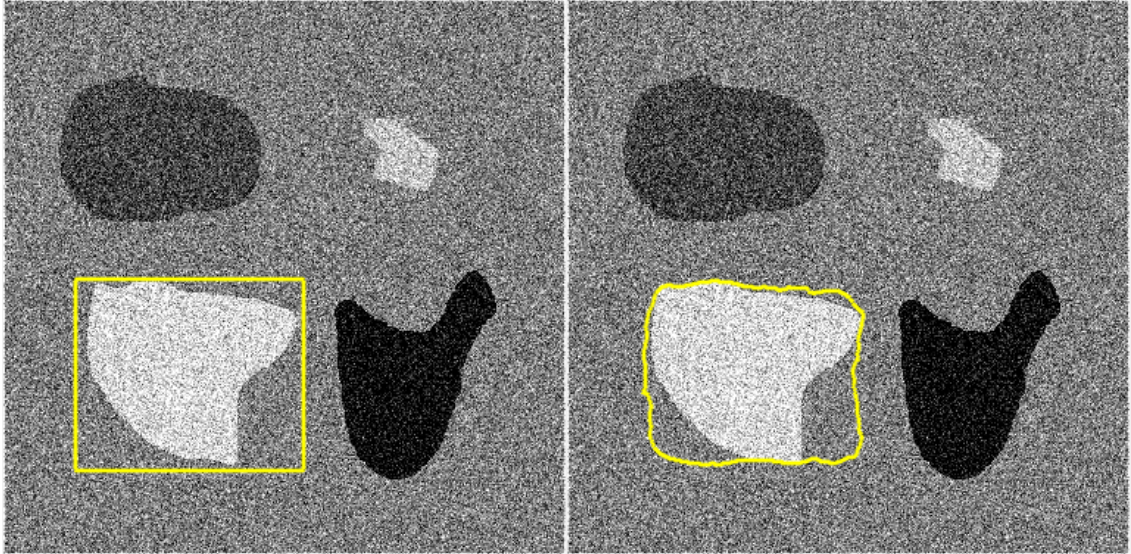


Figure 3.11: Effect of noise. Noise removal techniques ought to be implemented before segmentation.

3.6.3 Sensitivity to Noise

We have shown that our segmentation model enjoys great versatility in terms of the class of images it can process and its scope to multimodal images. Its main limitation is perhaps its sensitivity to noisy features in images. Being a hybrid model, spurious objects can significantly hamper its effectiveness as such anomalies are interpreted as possible boundaries of an object by the edge function g , Fig. 3.11. Therefore, preprocessing of noisy images using noise removal techniques [45, 46] is recommended before the implementation of our variational model.

CHAPTER 4

LESION DETECTION IN DERMOSCOPY IMAGES

As we have shown in Chapters 2 and 3, our hybrid models significantly enlarge the scope of region/edge exclusive models. We now turn our attention to a more specific class of images: skin lesions. In particular, this chapter focuses on how our hybrid models can be used in the segmentation and detection of lesions of the skin in Dermoscopy (also Dermatoscopy) images.

Dermatologists rely on dermoscopy images to distinguish benign skin lesions from malignant ones, most prominently a type of cancer known as *Melanoma*, which is the third most common manifestation of skin cancer and the most aggressive [61]. Due to the high incidence and mortality rates of melanoma, and the advancement of skin imaging acquisition technology, dermoscopy imagery has received a lot of attention from researchers over the past 15 years. However, there is still a need for computerized image analysis systems to minimize misdiagnoses and subjectivity of naked-eye interpretation [48].

To diagnose melanoma and other types of malignant pathologies using computer-aided approaches, an accurate separation of the lesion is of paramount importance. Once a successful segmentation is obtained, it is possible to classify skin lesions from their morphology (shape, symmetry or lack thereof, etc.) and other attributes [56]. Segmentation of dermoscopy images, however, is not without its challenges. For example, there exists several lesion types (melanomas, basal cell carcinomas, nevi, and others) that range significantly in shape and color, and often feature ambiguous boundaries, Fig. 4.1. Also, very frequently *noisy* features rear make un-

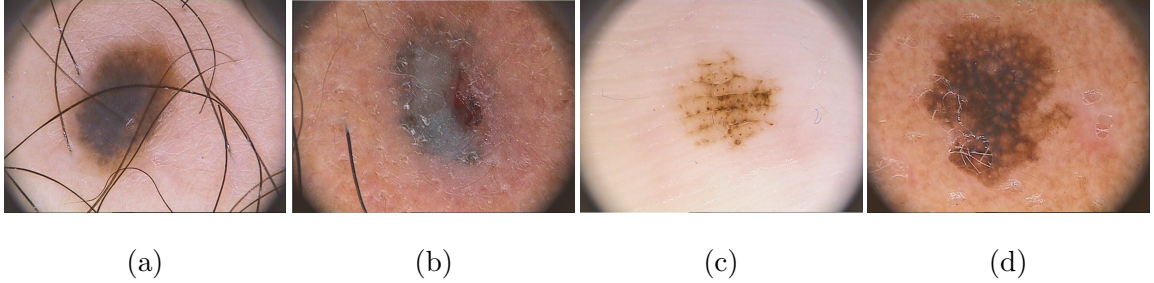


Figure 4.1: Some of the challenges of dermoscopy image segmentation: (a) hair, (b) variation in color, (c) ambiguous boundaries, (d) bubbles and other skin irregularities. Note also the invariable presence of the dark regions on the periphery of the images.

desirable appearances—most notably hair, bubbles and other skin irregularities, and dark regions on the periphery of the images.

4.1 Segmentation of Dermoscopy Images

A review of the literature reveals segmentation schemes that most computational biologists and other researchers have proposed typically consist of a number of steps [8, 18, 42, 48, 60]:

1. Pre-processing. This step seeks to remove a number of potentially problematic segments of the image such as the microscope border. Further, image smoothing is often performed to remove faulty skin texture, bubbles, and hair. Moreover, tasks such as color quantization that reduce the number of colors in images are also implemented prior to the segmentation step [8].
2. Segmentation. The actual segmentation step is typically achieved using one or more techniques such as *region growing*, *thresholding*, and *split and merge*.
3. Post-processing. Further noise reduction, correction of nonuniform lighting, and inpainting is also performed [42, 60].

From the above discussion the reader can be convinced that these prevalent

segmentation approaches are quite complex. We propose a greatly simplified approach to the segmentation of dermoscopy imagery using hybrid models introduced in this thesis.

4.1.1 Proposed Methodology

Our approach for dermoscopy imagery segmentation is as follows:

1. Convert image to grayscale, if necessary. The only information our models need is intensity at each pixel \mathbf{x} .
2. Initialize evolving front surrounding the lesion. The closer the front is located to the lesion, the faster the convergence ought to be.
3. Evolve front using either PDE-based model (2.10) or the Edge-Mean Separation model (3.25).

We note that neither pre-processing nor post-processing tasks are needed in our proposed methodology as the images are not intrinsically modified when converted to grayscale.

4.1.2 Performance Metric

By evolving an initial front C_0 to steady state using either (2.10) or (3.25) yields the region of interest (ROI) of an dermoscopy image I . We identify interior points to the final front as the potential ROI containing the skin lesion. To measure the accuracy of the ROI rendered by a model we define a metric that quantizes the number of mislabeled pixels \mathbf{x} of the image domain Ω .

Let $F : \Omega \rightarrow \{0, 1\}$ be a mapping labeling each pixel $\mathbf{x} \in \Omega$ as either in the potential ROI, $F(\mathbf{x}) = 1$, or not in the ROI, $F(\mathbf{x}) = 0$. Similarly, we define the “ground truth”

mapping $G : \Omega \rightarrow \{0, 1\}$ which provides the correct segmentation provided by an expert. We define the error ε in the segmentation F with respect to G as:

$$\varepsilon(F, G) = \frac{\sum_{\mathbf{x} \in \Omega} H(\mathbf{x})}{\sum_{\mathbf{x} \in \Omega} G(\mathbf{x})} \quad (4.1)$$

where

$$H(\mathbf{x}) = \begin{cases} 1, & F(\mathbf{x}) \neq G(\mathbf{x}) \\ 0, & F(\mathbf{x}) = G(\mathbf{x}) \end{cases}. \quad (4.2)$$

The function H compares the labeling $F(\mathbf{x})$ with $G(\mathbf{x})$ and returns 1 if they disagree. The number of mislabelings is counted and normalized by the total number of pixels in the ROI for the mapping G thus providing a measurement of the error carried by the ROI for mapping F . Note that $\varepsilon \in [0, 1]$; an error measure $\varepsilon = 0$ indicates perfect agreement between the labelings F and G , whereas $\varepsilon = 1$ indicates total mismatch of the labelings. Other possible metrics could also be employed [24].

4.2 Simulations

We benchmark our approach to dermoscopy image segmentation using images from PH² dataset [39]. The dataset consists of 200 images of melanocytic lesions, including 80 common nevi, 80 atypical nevi, and 40 melanomas. Medical segmentation of the lesions by an expert dermatologist are included in the dataset. For metric (4.1) values in the interval $[0, 0.15]$ are considered satisfactory [42].

For our first experiment we consider an image with a very undesirable pathology: significant presence of thick hair covering the lesion. To overcome this using deformable models without prior preprocessing, a judicious choice for the initial front is crucial. Because the front is propagated in the normal direction, the initial curve is chosen so that it “cuts off” each of the hairs perpendicularly. Even in the presence of such unwanted feature a segmentation is obtained with a 0.106 error using flow (3.25), Fig. 4.2. Images with thinner hair can be handled easily by our

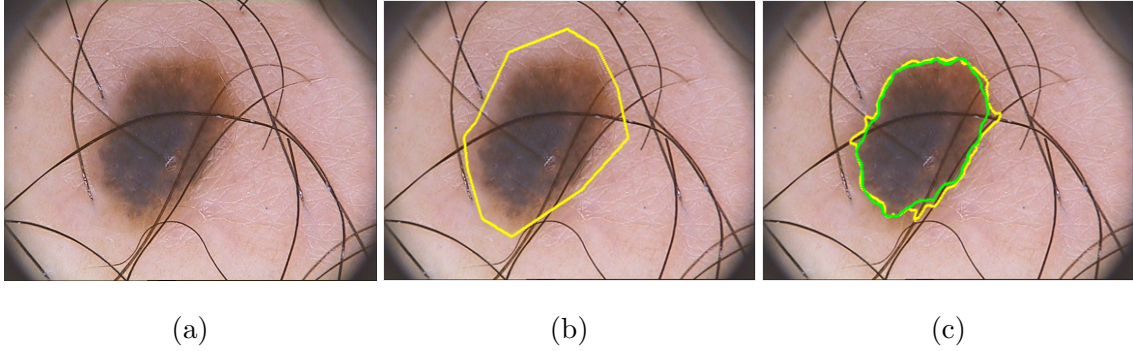


Figure 4.2: Dermoscopy image with thick hair. (a) Original, (b) initialization, and (c) final result in yellow and ground truth in green. Error in segmentation: 0.106.

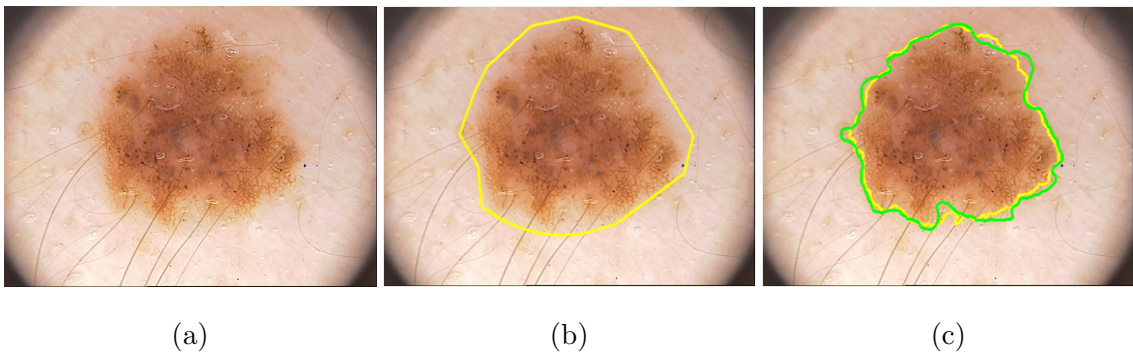
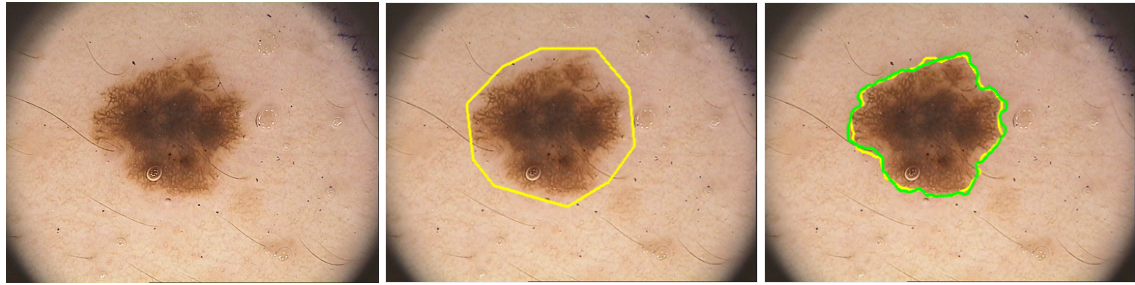


Figure 4.3: Dermoscopy image with thin hair. (a) Original, (b) initialization, and (c) final result in yellow and ground truth in green. Error in segmentation: 0.077.

models as shown in Fig. 4.3 . The same strategy is implemented by cutting the hairs perpendicularly with the initial curve and letting it evolve in the normal direction.

As the quality of the images improve in terms of hair presence, the accuracy of the results is elevated in proportion, Fig. 4.4. Note also the presence of bubbles and irregular spots around the lesion. All of these pathologies are overcome by a careful selection of the initial evolving curve.

Figure 4.5 shows the result of a segmented lesion with surrounding irregular skin. Such backgrounds require a higher number of iterations. A highly accurate segmentation is obtained with an error score of 0.079. The lesion in Fig. 4.6 features a somewhat ambiguous boundary. Our model is able to delineate the lesion boundary with 93% match to the expert's.



(a)

(b)

(c)

Figure 4.4: Dermoscopy image with thin hair and bubbles. (a) Original, (b) initialization, and (c) final result in yellow and ground truth in green. Error in segmentation: 0.055.



(a)

(b)

(c)

Figure 4.5: Dermoscopy image with thin hair. (a) Original, (b) initialization, and (c) final result in yellow and ground truth in green. Error in segmentation: 0.079.

For our last experiment we consider a dermoscopy image that poses a number of challenges. First, it has some imperfections due to reflection of the light emanating from the source. Second, it presents bubbles due to addition of a foreign substance prior to the image acquisition step. And finally, the lesion itself consists of several segments of different colors. Despite all these pathologies occurring in unison, a 90.7% accurate segmentation is obtained without any pre- or post-processing. Results for all experiments are summarized in Table 4.1.

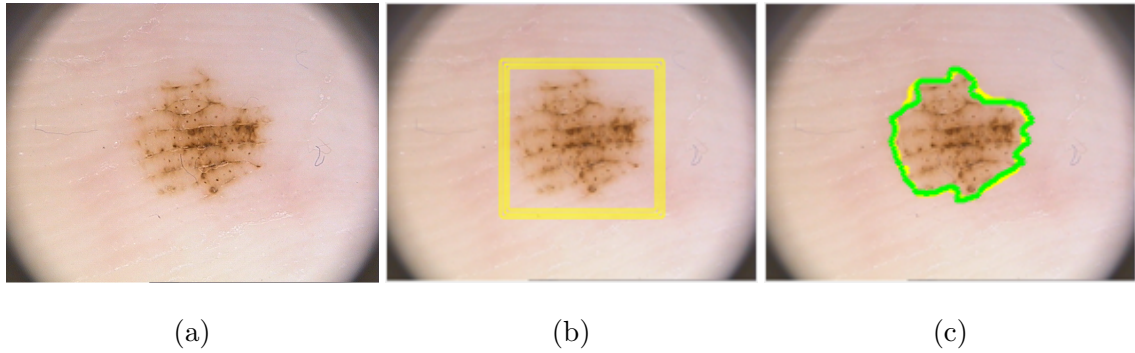


Figure 4.6: Dermoscopy image of lesion with ambiguous boundary. (a) Original, (b) initialization, and (c) final result in yellow and ground truth in green. Error in segmentation: 0.079.

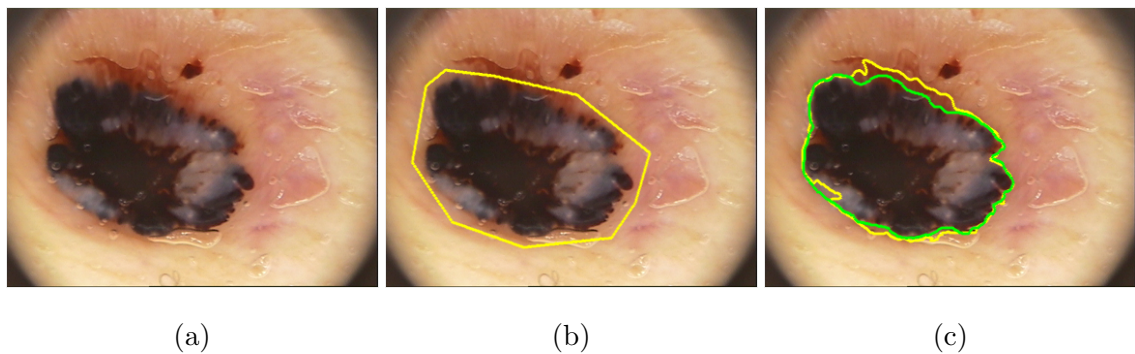


Figure 4.7: Dermoscopy image of lesion with significant color variation. (a) Original, (b) initialization, and (c) final result in yellow and ground truth in green. Error in segmentation: 0.093.

Image	Pathology	ε
Fig. 4.2	thick hair	0.106
Fig. 4.3	thin hair	0.077
Fig. 4.4	sparse hair	0.055
Fig. 4.5	irregular skin	0.079
Fig. 4.6	ambiguous lesion boundary	0.079
Fig. 4.7	multicolored, bubbles, glare	0.093

Table 4.1 – Segmentation error for images considered in this chapter.

CHAPTER 5

CONCLUSIONS AND FUTURE RESEARCH

In this dissertation we have contributed two mathematical models that aim to solve the problem of image segmentation for a large family of images. Starting from a number of assumptions about the composition of the images, we proposed our first model by specifying a differential equation directly whose steady state leads to the segmentation of the given image. Our second model was obtained from a variational formulation. Both models successfully take advantage of two different kinds of image data: *edge* information provides a criterion for slowing down the evolution of evolving fronts, whereas *region* information provides the direction for the evolution. We explored their strengths and identified their weaknesses through experimentation using synthetic and real images. In particular, our models are not able to separate objects with different graylevel modalities. We presume n -modal images, $n > 1$, require n evolving fronts to detect each intensity modality. This is a natural generalization that we intend to investigate further. Finally we applied our models to segment skin lesions in dermoscopy images with promising results.

Both proposed models ultimately lead to nonlinear partial differential equations whose solutions were approximated using finite differences. Although these approximations are chosen most often by researchers, there are other methods that can be explored, namely finite-element methods, finite-volume methods, and spectral methods [55]. A natural question that arises is: how effective these alternate methods are, and can formal mathematical results be obtained? When using any numerical scheme to obtain approximate solutions of equations one is interested in

providing an answer the following questions:

1. **Consistency:** How well the numerical scheme approximates the underlying PDE.
2. **Convergence:** How close to the exact solution are the solutions of the chosen numerical scheme.
3. **Stability:** A sort of well-posedness condition for the discretized problems, it establishes that solutions of a numerical scheme associated to certain initial data should remain close to solutions associated to the same initial data slightly perturbed.

With the exception of a handful of models, answers to these questions are typically avoided.

Alternatively, one could seek to obtain an existence result directly from the intrinsic characteristics of the numerical scheme using classical fixed point theory. This requires care, as the manner in which the finite difference (or other) approximations are constructed (forward, backwards, centered, etc.) and the norm used to obtain the estimates can affect the well-posedness of the problem. Unfortunately, we cannot guarantee uniqueness of solutions due to lack of convexity of the functionals, but this is not a major drawback as it relates to the practical results one seeks in image segmentation problems as long as meaningful partition of images are obtained. The standard approach is as follows:

1. Choose a grid of $N \times N$ equally spaced points $(x_i, y_i) = (ih, jh) \in \Omega, i, j = 1, 2, \dots, N$, and $h > 0$.
2. Define $\phi_{ij}^0 \approx \phi(0, ih, jh), i, j = 1, 2, \dots, N$.
3. Given ϕ_{ij}^n , compute ϕ_{ij}^{n+1} as the solution of a predefined numerical scheme.

4. Show that the sequence (ϕ_{ij}^n) thus obtained converges for $n \rightarrow \infty$. This limit is the approximate solution of the original PDE.

Often, however, the estimates required to obtain the above results prove difficult to be realized. We intend to investigate these matters in future research work.

REFERENCES

- [1] David Adalsteinsson and James A Sethian, *A fast level set method for propagating interfaces*, Journal of computational physics **118** (1995), no. 2, 269–277.
- [2] Luis Alvarez, Frédéric Guichard, Pierre-Louis Lions, and Jean-Michel Morel, *Axioms and fundamental equations of image processing*, Archive for Rational Mechanics and Analysis **123** (1993), no. 3, 199–257.
- [3] Luis Alvarez, Pierre-Louis Lions, and Jean-Michel Morel, *Image selective smoothing and edge detection by nonlinear diffusion. ii*, SIAM Journal on numerical analysis **29** (1992), no. 3, 845–866.
- [4] Gilles Aubert and Pierre Kornprobst, *Mathematical problems in image processing: partial differential equations and the calculus of variations*, Vol. 147, Springer Science & Business Media, 2006.
- [5] Gilles Aubert, Barlaud Michel, Olivier Faugeras, and Stéphanie Jehan-Besson, *Image segmentation using active contours: Calculus of variations or shape gradients?*, SIAM Journal on Applied Mathematics **63** (2003), no. 6, 2128–2154.
- [6] Vicent Caselles, Francine Catté, Tomeu Coll, and Françoise Dibos, *A geometric model for active contours in image processing*, Numerische Mathematik **66** (1993), no. 1, 1–31.
- [7] Vicent Caselles, Ron Kimmel, and Guillermo Sapiro, *Geodesic active contours*, International journal of computer vision **22** (1997), no. 1, 61–79.
- [8] M. E. Celebi and A. Zornberg, *Automated quantification of clinically significant colors in dermoscopy images and its application to skin lesion classification*, IEEE Systems Journal **8** (2014), no. 3, 980–984.
- [9] Tony F Chan and Luminita A Vese, *Active contours without edges*, Image processing, IEEE transactions on **10** (2001), no. 2, 266–277.

- [10] Bo Chen, Qing-Hua Zou, Wen-Sheng Chen, and Bin-Bin Pan, *A novel adaptive partial differential equation model for image segmentation*, *Applicable Analysis* **93** (2014), no. 11, 2440–2450.
- [11] Laurent D Cohen, *On active contour models and balloons*, *CVGIP: Image understanding* **53** (1991), no. 2, 211–218.
- [12] Richard Courant, Kurt Friedrichs, and Hans Lewy, *ber die partiellen differenzgleichungen der mathematischen physik*, *Mathematische Annalen* **100** (1928), no. 1, 32–74.
- [13] Michael G Crandall, Lawrence C Evans, and P-L Lions, *Some properties of viscosity solutions of hamilton-jacobi equations*, *Transactions of the American Mathematical Society* **282** (1984), no. 2, 487–502.
- [14] Michael G Crandall, Hitoshi Ishii, and Pierre-Louis Lions, *User's guide to viscosity solutions of second order partial differential equations*, *Bulletin of the American Mathematical Society* **27** (1992), no. 1, 1–67.
- [15] Michael G Crandall and Pierre-Louis Lions, *Viscosity solutions of hamilton-jacobi equations*, *Transactions of the American Mathematical Society* **277** (1983), no. 1, 1–42.
- [16] Gérard De Vaucouleurs, *Classification and morphology of external galaxies*, *Astrophysik iv: Sternsysteme/astrophysics iv: Stellar systems*, 1959, pp. 275–310.
- [17] Omer Demirkaya, Musa Hakan Asyali, and Prasanna Sahoo, *Image processing with matlab : applications in medicine and biology*, CRC Press, Boca Raton, 2009.
- [18] M Emre Celebi, Y Alp Aslandogan, William V Stoecker, Hitoshi Iyatomi, Hiroshi Oka, and Xiaohe Chen, *Unsupervised border detection in dermoscopy images*, *Skin Research and Technology* **13** (2007), no. 4, 454–462.
- [19] CL Epstein and Michael Gage, *The curve shortening flow*, *Wave motion: theory, modelling, and computation* (1987), 15–59.
- [20] Lawrence C. Evans, *On solving certain nonlinear partial differential equations by accretive operator methods*, *Israel Journal of Mathematics* **36** (1980), no. 3-4, 225–247.
- [21] ———, *Partial differential equations*, *Graduate studies in mathematics*, American Mathematical Society, Providence, R.I., 1998.
- [22] Lawrence C. Evans and Joel Spruck, *Motion of level sets by mean curvature I*, *J. Diff. Geom* **33** (1991), no. 3, 635–681.

- [23] Aly A. Farag, *Biomedical image analysis: Statistical and variational methods*, Cambridge Univ Press, Cambridge, 2014.
- [24] Tom Fawcett, *An introduction to roc analysis*, Pattern Recognition Letters **27** (2006), no. 8, 861–874.
- [25] Rafael Garcia, Tudor Nicosevici, and Xevi Cuf?, *On the way to solve lighting problems in underwater imaging*, Oceans'02 mts/ieee, 2002, pp. 1018–1024.
- [26] Rafael C. Gonzalez, Richard E. Woods, and Steven L. Eddins, *Digital image processing using matlab*, Pearson Prentice Hall, Upper Saddle River, N. J., 2004.
- [27] Michael Kass, Andrew Witkin, and Demetri Terzopoulos, *Snakes: Active contour models*, International journal of computer vision **1** (1988), no. 4, 321–331.
- [28] Satyanad Kichenassamy, Arun Kumar, Peter Olver, Allen Tannenbaum, and Anthony Yezzi, *Gradient flows and geometric active contour models*, Computer vision, 1995. proceedings., fifth international conference on, pp. 810–815.
- [29] Satyanad Kichenassamy, Arun Kumar, Peter Olver, Allen Tannenbaum, and Anthony Yezzi Jr, *Conformal curvature flows: from phase transitions to active vision*, Archive for Rational Mechanics and Analysis **134** (1996), no. 3, 275–301.
- [30] Shawn Lankton, Delphine Nain, Anthony Yezzi, and Allen Tannenbaum, *Hybrid geodesic region-based curve evolutions for image segmentation*, Medical Imaging (2007), 65104U–65104U–10.
- [31] Shawn Lankton and Allen Tannenbaum, *Localizing region-based active contours*, Image Processing, IEEE Transactions on **17** (2008), no. 11, 2029–2039.
- [32] Chunming Li, Rui Huang, Zhaohua Ding, J Chris Gatenby, Dimitris N Metaxas, and John C Gore, *A level set method for image segmentation in the presence of intensity inhomogeneities with application to MRI*, Image Processing, IEEE Transactions on **20** (2011), no. 7, 2007–2016. Metrics.
- [33] Chunming Li, Chenyang Xu, Changfeng Gui, and Martin D Fox, *Level set evolution without re-initialization: a new variational formulation*, IEEE Computer Society Conference on Computer Vision and Pattern Recognition **1** (2005), 430–436.
- [34] ———, *Distance regularized level set evolution and its application to image segmentation*, Image Processing, IEEE Transactions on **19** (2010), no. 12, 3243–3254.

- [35] Bostjan Likar, JB Antoine Maintz, Max A Viergever, and F Pernus, *Retrospective shading correction based on entropy minimization*, Journal of Microscopy **197** (2000), no. 3, 285–295.
- [36] R. Malladi, J. A. Sethian, and B. C. Vemuri, *Shape modeling with front propagation: a level set approach*, Pattern Analysis and Machine Intelligence, IEEE Transactions on **17** (1995), no. 2, 158–175.
- [37] Oge Marques, *Practical image and video processing using matlab*, Wiley-IEEE Press, Hoboken, NJ, 2011.
- [38] David Marr and Ellen Hildreth, *Theory of edge detection*, Proceedings of the Royal Society of London B: Biological Sciences **207** (1980), no. 1167, 187–217.
- [39] T. Mendona, P. M. Ferreira, J. S. Marques, A. R. S. Marcal, and J. Rozeira, *Ph2 - a dermoscopic image database for research and benchmarking*, 2013 35th annual international conference of the ieee engineering in medicine and biology society (embc), pp. 5437–5440.
- [40] Donald G. Mitchell, *Mri principles*, Saunders, Philadelphia, 1999.
- [41] David Mumford and Jayant Shah, *Optimal approximations by piecewise smooth functions and associated variational problems*, Communications on pure and applied mathematics **42** (1989), no. 5, 577–685.
- [42] Kerri-Ann Norton, Hitoshi Iyatomi, M Emre Celebi, Gerald Schaefer, Masaru Tanaka, and Koichi Ogawa, *Development of a novel border detection method for melanocytic and non-melanocytic dermoscopy images*, Engineering in medicine and biology society (embc), 2010 annual international conference of the ieee, pp. 5403–5406.
- [43] Stanley Osher and Ronald P. Fedkiw, *Level set methods and dynamic implicit surfaces*, Springer, New York, 2003.
- [44] Stanley Osher and James A. Sethian, *Fronts propagating with curvature-dependent speed: algorithms based on hamilton-jacobi formulations*, Journal of computational physics **79** (1988), no. 1, 12–49.
- [45] Pietro Perona, Takahiro Shiota, and Jitendra Malik, *Anisotropic diffusion*, Geometry-driven diffusion in computer vision, 1994, pp. 73–92.
- [46] Leonid I Rudin, Stanley Osher, and Emad Fatemi, *Nonlinear total variation based noise removal algorithms*, Physica D: Nonlinear Phenomena **60** (1992), no. 1, 259–268.

- [47] Guillermo Sapiro, *Geometric partial differential equations and image analysis*, Cambridge University Press, Cambridge ; New York, 2001.
- [48] Gerald Schaefer, Bartosz Krawczyk, M Emre Celebi, and Hitoshi Iyatomi, *Melanoma classification using dermoscopy imaging and ensemble learning*, Pattern recognition (acpr), 2013 2nd iapr asian conference on, pp. 386–390.
- [49] James A. Sethian, *Curvature and the evolution of fronts*, Communications of Mathematical Physics **101** (1985), 487–499.
- [50] ———, *Numerical algorithms for propagating interfaces: Hamilton-jacobi equations and conservation laws*, Journal of differential geometry **31** (1990), no. 1, 131–161.
- [51] ———, *Level set methods and fast marching methods: evolving interfaces in computational geometry, fluid mechanics, computer vision, and materials science*, Vol. 3, Cambridge university press, 1999.
- [52] James A Sethian, *Evolution, implementation, and application of level set and fast marching methods for advancing fronts*, Journal of Computational Physics **169** (2001), no. 2, 503–555.
- [53] Gilbert Strang, *Introduction to applied mathematics*, Wellesley-Cambridge Press, Wellesley, Mass., 1986.
- [54] Mark Sussman, Peter Smereka, and Stanley Osher, *A level set approach for computing solutions to incompressible two-phase flow*, Journal of Computational physics **114** (1994), no. 1, 146–159. Initialization of distance function.
- [55] Eitan Tadmor, *A review of numerical methods for nonlinear partial differential equations*, Bulletin of the American Mathematical Society **49** (2012), no. 4, 507–554.
- [56] Masaru Tanaka, *Dermoscopy*, The Journal of Dermatology **33** (2006), no. 8, 513–517.
- [57] Tran Thi-Thao, Pham Van-Truong, Chiu Yun-Jen, and Shyu Kuo-Kai, *Active contour with selective local or global segmentation for intensity inhomogeneous image*, 3rd IEEE International Conference on Computer Science and Information Technology (ICCSIT) **1** (2010), 306–310.
- [58] Andrey Nikolaevich Tikhonov and Vasiliy Yakovlevich Arsenin, *Solutions of ill-posed problems*, Vh Winston, 1977.
- [59] Dejan Tomazevic, Bostjan Likar, and Franjo Pernus, *Comparative evaluation of retrospective shading correction methods*, Journal of Microscopy **208** (2002), no. 3, 212–223.

- [60] Mohammad Taghi Bahreyni Toossi, Hamid Reza Pourreza, Hoda Zare, Mohamad-Hoseyn Sigari, Pouran Layegh, and Abbas Azimi, *An effective hair removal algorithm for dermoscopy images*, *Skin Research and Technology* **19** (2013), no. 3, 230–235.
- [61] Richard Usatine, Mindy A. Smith, E. J. Jr. Mayeaux, and Heidi S. Chumley, *Chapter 172: Melanoma*, *The color atlas of family medicine*, 2013.
- [62] Andrew Webb, *Introduction to biomedical imaging*, Wiley-Interscience, Hoboken, N.J., 2003.
- [63] Haiyong Xu, Tingting Liu, and Guotao Wang, *Hybrid geodesic region-based active contours for image segmentation*, *Computers & Electrical Engineering* **40** (2014), no. 3, 858–869.
- [64] A. Yezzi, A. Tsai, and A. Willsky, *A statistical approach to snakes for bimodal and trimodal imagery*, *Computer vision, 1999. the proceedings of the seventh ieee international conference on*, pp. 898–903 vol.2.
- [65] Anthony Yezzi, Andy Tsai, and Alan Willsky, *A fully global approach to image segmentation via coupled curve evolution equations*, *Journal of Visual Communication and Image Representation* **13** (2002), no. 1, 195–216.
- [66] Kaihua Zhang, Lei Zhang, Huihui Song, and Wengang Zhou, *Active contours with selective local or global segmentation: a new formulation and level set method*, *Image and Vision computing* **28** (2010), no. 4, 668–676.
- [67] Song Chun Zhu and Alan Yuille, *Region competition: Unifying snakes, region growing, and bayes/mdl for multiband image segmentation*, *Pattern Analysis and Machine Intelligence, IEEE Transactions on* **18** (1996), no. 9, 884–900.

APPENDIX A MATLAB CODE

A.1 PDE-based Model

```
1 function c1 = pdebased_seg(I, c1, n, dt, sigma, alpha, rho, refresh, nu, ~, ~)
```

Description of function arguments:

- `I` is the image I to be segmented with dimensions `row` by `col`.
- `c1` is the initial curve in level set form, which corresponds to u_0 .
- `n` corresponds to the maximum number of iterations the loop is to run.
- `dt` corresponds to the time step Δt .
- `sigma`, the standard deviation σ for the Gaussian kernel
- `alpha` is the overall propagation speed $\alpha > 0$.
- `rho` is the size of the localization parameter ρ . Smaller values of `sizew` increase the localization property of the method.
- `nu` controls *stretching* of the exponential weights w_1, w_2 (2.8).
- `rfsh` and `lnclr` control the frequency outputs are displayed, and the color of contours shown on screen, respectively.

Error Handling

The following are error handling routines that ensure the function is able to run with at least the default parameters.

```

2 %Maximum number of iterations set to 200.
3 if(~exist('n','var'))
4     n = 200;
5 end
6
7 %Propagation speed alpha set to unit speed.
8 if(~exist('alpha','var'))
9     alpha = 1;
10 end
11
12 %Time step increment dt = 1.
13 if(~exist('dt','var'))
14     dt = 1;end
15
16 %Standard deviation sigma =1
17 if(~exist('sigma','var'))
18     sigma = 1;end
19
20 %Size of localization window rho
21 if(~exist('rho','var'))
22     rho = 20;
23 end
24
25 %Parameter for the exponential weights nu
26 if(~exist('nu','var'))
27     nu = 1;
28 end
29
30 %Refresh output every 20 iterations
31 if(~exist('refresh','var'))
32     refresh = 20;end

```

Initialization steps

```
33 % Get size of image to be segmented
34 [row, col, ~] = size(I); %Only 2-D images are considered
35 % Getting working image
36 J=get_working_image(I);
```

“Filter” definitions

```
37 %Gradient map for input image used in exponential weights (eq. 2.4)
38 gradj=gradmag(J);
39 %Exponential weights from equation (2.4)
40 a=1-exp(-gradj/nu); b=1-a;
```

Loop

```
41 for i=1:dt:n
42     %% Boundary conditions
43     % We verify the Neumann boundary conditions are before the
44     % evolutionary process at the beginning of each iteration.
45     % See 'Subfunction: Boundary Conditions' below.
46     c1=Boundarycond(c1,row,col);
47     %% Operate on narrow band
48     %capture the pixels using indexes i
49     idx = find(c1 <= 1.2 & c1 >= -1.2)';
50     %% Evolution
51     % See subfunctions for computation of Global and Local stats.
52     c1(idx)=c1(idx)+alpha*dt.*(b(idx).*global_means(J,c1,idx)+...
53         a(idx).*local_means(J,idx,c1,rho));
54     % Regularization step (Convolution with Gaussian kernel)
55     c1=imgaussfilt(c1, sigma); show_evolution(I,c1,i,refresh);
56 end end
```

Auxiliary Functions

```
57 %% Subfunction: Boundary Conditions
58 function g = Boundarycond(f, row, col)
59     f([1 row],[1 col]) = f([3 row-2],[3 col-2]);%top corners
60     f(2:end-1,1)=f(2:end-1,2);                %left edge
61     f(2:end-1,end)=f(2:end-1,end-1);          %right edge
62     f(1,2:end-1)=f(2,2:end-1);                %top edge
63     f(end,2:end-1)=f(end-1,2:end-1);          %bottom edge
64     g = f;
65 end
66 %% Subfunction: Global Statistical information from image
67 % Corresponds to functional  $F.G(\cdot, \cdot)$  from eq. (2.4)
68 function g1 = global.means(J,c1,idx)
69     inidx = (c1>=0);    %Get pixels inside interface
70     outidx = (c1<0);    %Get pixels outside interface
71     c10 = sum(J(inidx))/(sum(inidx(:))+eps);    %average inside
72     c2 = sum(J(outidx))/(sum(outidx(:))+eps);  %average outside
73     num=2*J(idx)-(c10+c2); %Computation of operator
74     d=max(max(abs(num)))+eps; %Computation of maximum
75     g1=num/d; %Normalization
76 end
77 %% Subfunction: Local Statistical information from image
78 % Corresponds to functional  $F.L(\cdot, \cdot)$  from eq. (2.4)
79 function h1=local.means(J,idx,c1,rho)
80     [dimy, dimx] = size(J);
81     [y, x] = ind2sub(size(c1),idx);
82     xneg = x-rho; xpos = x+rho; %get subscripts for local regions
83     yneg = y-rho; ypos = y+rho;
84     xneg(xneg<1)=1; yneg(yneg<1)=1; %check bounds
85     xpos(xpos>dimx)=dimx; ypos(ypos>dimy)=dimy;
```

```

86     %Make space in memory for variables mean1, mean2, sum1, sum2
87     mean1=zeros(size(idx)); mean2=mean1;
88     sum1=mean1; sum2=sum1;
89     for i = 1:numel(idx) % Get points on the narrow band
90         img = J(yneg(i):ypos(i),xneg(i):xpos(i)); %on the image
91         P = c1(yneg(i):ypos(i),xneg(i):xpos(i)); %on the front
92
93         pts1 = find(P<=0);
94         sum1(i) = length(pts1)+eps;
95         mean1(i) = sum(img(pts1))/sum1(i);
96
97         pts2 = find(P>0);
98         sum2(i) = length(pts2)+eps;
99         mean2(i) = sum(img(pts2))/sum2(i);
100    end
101    h1=J(idx)-(u+v)*.5; % Computation along the narrow band
102    h1=h1/max(max(h1)); % Normalization
103 end
104 %% Subfunction: Visualization
105 % Visualizing the results at the current iteration.
106 function show_evolution(I,c1,i,refresh)
107     if mod(i,refresh)==0
108         subplot(2,2,3);
109         imagesc(I,[0 255]); axis off; colormap(gray);hold on;
110         [~, ~] = contour(c1, [0 0], 'y','LineWidth',2);
111         contour(c1, [0 0], 'k','LineWidth',1);
112         iterNum = [num2str(i), ' iterations'];
113         title(iterNum);pause(.2);
114         hold off;
115     end
116 end

```

```

118 %% Subfunction: Getting working image
119 function J=get_working_image(I)
120 if size(I,3)== 3    %Should the image be a color image
121     J = double(rgb2gray(uint8(I))); %rgb and 8 bit integer (0-255)
122 elseif size(I,3) == 2
123     J = 0.5.*(double(I(:,:,1))+double(I(:,:,2)));
124 else
125     J = im2double(I);    %convert to double otherwise
126 end
127 end

```

A.2 Variational Model

```

1 function seg = variational_seg(I,c1,n,alpha,sigma)

```

Description of function arguments:

- I is the image I to be segmented with dimensions `row` by `col`.
- `c1` is the initial curve in level set form, which corresponds to u_0 .
- `n` corresponds to the maximum number of iterations the loop is to run.
- `sigma`, the standard deviation σ for the Gaussian kernel
- `alpha` is the overall propagation speed $\alpha > 0$.

Error Handling

As before, we make sure execution is possible using default parameters.

```

2 if(~exist('alpha','var')), alpha = 1;end %Arclength parameter
3 if(~exist('sigma','var')), sigma = 1;end %Standard deviation

```

Initialization steps

```
4 % Getting working image
5 J=get_working_image(I);
6 c1 = mask2phi(c1);% c1 Distance transform
7 % Edge function
8 g=imgaussfilt(I, sigma); %First smooth the image
9 [FX,FY] = gradient(g); %Compture gradient map
10 g = sqrt(FX.^2+FY.^2+eps); %eps added to avoid division by zero
11 g = 1 ./ ( 1 + g.^2 );
```

Loop

```
12 for i = 1:n
13 % Get indices for narrow band
14 idx = find(c1 <= 1.2 & c1 >= -1.2)';
15 [y, x] = ind2sub(size(c1),idx); %Rectangular coords line 14
16 sum(J(inidx))/(sum(inidx(:))+eps);
17 mean1=sum(J(c1<0))/(length(J(c1<0))+eps);sum1=length(J(c1<0))+eps;
18 mean2=sum(J(c1>=0))/(length(J(c1>=0))+eps);sum2=length(J(c1>=0))+eps;
19 curvature = get_curvature(c1,idx,x,y);
20 F = -g(idx).*((mean1-mean2).*(J(idx)-mean1)./...
21 sum1+(J(idx)-mean2)./sum2));
22 rhs = F./max(abs(F)) + alpha*curvature;
```

CFL condition [12] for stability:

```
23 dt = .45/(max(rhs)+eps);
```

```
24 %% Evolution
25 c1(idx) = c1(idx) + dt.*rhs;
26 c1 = sussman(c1, .5); %Regularization of c1 \cite{Sussman94}
27 show_evolution(I,c1,i,refresh);end,show_evolution(I,c1,i,refresh)
28 seg = c1<=0; %-- Get mask from levelset
```

Auxiliary Functions

```
29 %% Subfunction: Visualization
30 function show_evolution(I,c1,i,refresh)
31     if mod(i,refresh)==0
32         subplot(2,2,3);
33         imagesc(I,[0 255]); axis off; colormap(gray);hold on;
34         [~, ~] = contour(c1, [0 0], 'y','LineWidth',2);
35         contour(c1, [0 0], 'k','LineWidth',1);
36         iterNum = [num2str(i), ' iterations'];
37         title(iterNum);
38         pause(.2);
39         hold off;
40     end
41 %% Subfunction: Conversion of logical mask to SDF
42 % Logical masks have value of 1 inside the front and zero outside
43 function phi = mask2phi(c)
44     phi=bwdist(c)-bwdist(1-c)+im2double(c)-.5;
```

The following are standard lines of code for level set reinitialization [54].

```
45 % Adapted from http://goo.gl/8pg4qf
46 function D = sussman(D, dt)
47     % forward/backward differences
48     a = D - shiftR(D); % backward
49     b = shiftL(D) - D; % forward
50     c = D - shiftD(D); % backward
51     d = shiftU(D) - D; % forward
52     a_p = a; a_n = a; % a+ and a-
53     b_p = b; b_n = b;
54     c_p = c; c_n = c;
55     d_p = d; d_n = d;
```



```

56  a_p(a < 0) = 0;
57  a_n(a > 0) = 0;
58  b_p(b < 0) = 0;
59  b_n(b > 0) = 0;
60  c_p(c < 0) = 0;
61  c_n(c > 0) = 0;
62  d_p(d < 0) = 0;
63  d_n(d > 0) = 0;
64  dD = zeros(size(D));
65  D_neg_ind = find(D < 0);
66  D_pos_ind = find(D > 0);
67  dD(D_pos_ind) = sqrt(max(a_p(D_pos_ind).^2, b_n(D_pos_ind).^2) ...
68                  + max(c_p(D_pos_ind).^2, d_n(D_pos_ind).^2)) - 1;
69  dD(D_neg_ind) = sqrt(max(a_n(D_neg_ind).^2, b_p(D_neg_ind).^2) ...
70                  + max(c_n(D_neg_ind).^2, d_p(D_neg_ind).^2)) - 1;
71  D = D - dt .* sussman_sign(D) .* dD;
72  %-- whole matrix derivatives
73  function shift = shiftD(M)
74  shift = shiftR(M)';
75
76  function shift = shiftL(M)
77  shift = [ M(:,2:size(M,2)) M(:,size(M,2)) ];
78
79  function shift = shiftR(M)
80  shift = [ M(:,1) M(:,1:size(M,2)-1) ];
81
82  function shift = shiftU(M)
83  shift = shiftL(M)';
84
85  function S = sussman_sign(D)
86  S = D ./ sqrt(D.^2 + 1);

```

```

87 %% Subfunction: Mean curvature computation
88 function curvature = get_curvature(phi, idx, x, y)
89     [dimy, dimx] = size(phi);
90     %%-- get subscripts of neighbors
91     ym1 = y-1; xm1 = x-1; yp1 = y+1; xp1 = x+1;
92     %%-- bounds checking
93     ym1(ym1<1) = 1; xm1(xm1<1) = 1;
94     yp1(yp1>dimy)=dimy; xp1(xp1>dimx) = dimx;
95     %%-- get indexes for 8 neighbors
96     idup = sub2ind(size(phi), yp1, x);
97     iddn = sub2ind(size(phi), ym1, x);
98     idlt = sub2ind(size(phi), y, xm1);
99     idrt = sub2ind(size(phi), y, xp1);
100    idul = sub2ind(size(phi), yp1, xm1);
101    idur = sub2ind(size(phi), yp1, xp1);
102    iddl = sub2ind(size(phi), ym1, xm1);
103    iddr = sub2ind(size(phi), ym1, xp1);
104    %%-- get central derivatives of SDF at x,y
105    phi_x = -phi(idlt)+phi(idrt);
106    phi_y = -phi(iddn)+phi(idup);
107    phi_xx = phi(idlt)-2*phi(idx)+phi(idrt);
108    phi_yy = phi(iddn)-2*phi(idx)+phi(idup);
109    phi_xy = -0.25*phi(iddl)-0.25*phi(idur)...
110            +0.25*phi(iddr)+0.25*phi(idul);
111    phi_x2 = phi_x.^2;
112    phi_y2 = phi_y.^2;
113    %%-- compute curvature (Kappa)
114    curvature = ((phi_x2.*phi_yy + phi_y2.*phi_xx...
115                - 2*phi_x.*phi_y.*phi_xy)./(phi_x2 + phi_y2 +eps).^ (3/2)).*...
116                (phi_x2 + phi_y2).^ (1/2);

```

```
116 %% System information
117 % MATLAB Version: 8.6.0.267246 (R2015b)
118 % OS: Microsoft Windows 10 Home Version 10.0 (Build 10586)
119 % Java Ver: Java 1.7.0_60-b19 w/ Oracle Corporation Java HotSpot (TM)
```

APPENDIX B
Frequently Used Symbols

Symbol	Meaning
\mathbb{R}	real line (set of real numbers)
\mathbb{R}^d	d - dimensional Euclidean space, commonly $d = 2$ or 3
∇	gradient vector field (of a function), divergence of vector fields
div	divergence of vector fields
∂D	boundary of the set D
$int(C)$	interior of the curve C
x_q, x_t	partial derivative of x with respect to q , and t
·	dot product of vectors
$\langle a, b \rangle$	2-dimensional vector with components a, b
Δ	Laplace operator
$\ \vec{V}\ $	Euclidean norm of the vector \vec{V}
*	convolution operator
$ \mathcal{U} $	Lebesgue measure of the set \mathcal{U}

CURRICULUM VITAE

Carlos M. Paniagua Mejía

328 Natural Sciences Building

University of Louisville

Louisville, KY 40292

cpaniguam@gmail.com

Education

- | | |
|-----------|---|
| 2016 | Ph.D. Mathematics, University of Louisville |
| 2012-2016 | Graduate Teaching Assistant
Department of Mathematics, University of Louisville, USA. |
| 2010-2012 | Fulbright Fellow
Department of Mathematics, University of Louisville, USA. |
| 2008 | M.A. in Mathematics
Instituto Tecnológico de Santo Domingo, Dominican Republic. |
| 2004 | B.S. in Electrical Engineering
Instituto Tecnológico de Santo Domingo, Dominican Republic. |

Research Interests

Partial Differential Equations, Nonlinear PDE, Applied Mathematics, Real Analysis, Image Processing